C: Energy Conversion and Storage; Energy and Charge Transport

Characterization of Electronic Transport through Amorphous TiO Produced by Atomic-Layer Deposition

Paul Nunez, Matthias H. Richter, Brandon D. Piercy, Christopher W. Roske, Miguel Cabán-Acevedo, Mark D Losego, Steven J. Konezny, David J. Fermin, Shu Hu, Bruce S. Brunschwig, and Nathan S. Lewis

J. Phys. Chem. C, **Just Accepted Manuscript** • DOI: 10.1021/acs.jpcc.9b04434 • Publication Date (Web): 19 Jun 2019

Characterization of Electronic Transport through Amorphous TiO_2 Produced by Atomic-Layer Deposition

Paul Nunez, [†] Matthias H. Richter, [†] Brandon D. Piercy, [‡] Christopher W. Roske, [†] Miguel Cabán-Acevedo, [†] Mark D. Losego, [‡] Steven J. Konezny, *[, §,∥] David J. Fermin, [⊥] Shu Hu, *[, §,#] Bruce S. Brunschwig, [▽] and Nathan S. Lewis *[,†, ▽]

[†] Division of Chemistry and Chemical Engineering, California Institute of Technology, Pasadena, California 91125, USA.

[‡] School of Materials Science and Engineering, Georgia Institute of Technology, Atlanta, GA 30332, USA.

[§] Energy Sciences Institute, Yale West Campus, West Haven, CT 06516, USA.

[∥] Department of Chemistry, Yale University, 225 Prospect Street, P.O. Box 208107, New Haven, Connecticut, 06520-8107, USA.

[⊥] School of Chemistry, University of Bristol, Cantock's Close, Bristol BS8 1TS, United Kingdom.

[#] Department of Chemical and Environmental Engineering, School of Engineering and Applied Sciences, Yale University, New Haven, CT 06520, USA.

[▽] Beckman Institute and Molecular Materials Research Center, California Institute of Technology, Pasadena, CA 91125, USA.

ABSTRACT:

The electrical transport in amorphous titanium dioxide (*a*-TiO_2) thin films deposited by atomic-layer deposition (ALD), and across heterojunctions of p^+-Si|*a*-TiO_2|metal substrates that had various top metal contacts, has been characterized by AC conductivity, temperature-dependent DC conductivity, space-charge-limited current (SCLC) spectroscopy, electron paramagnetic resonance (EPR), X-ray photoelectron spectroscopy (XPS), and current density versus voltage (*J-V*) characteristics. Amorphous TiO_2 films were fabricated using either tetrakis(dimethylamido)-titanium (TDMAT) with a substrate temperature of 150 °C or $TiCl_4$ with a substrate temperature of 50, 100, or 150 °C. EPR spectroscopy of the films showed that the Ti^{3+} concentration varied with the deposition conditions, and increases in the concentration of Ti^{3+} in the films correlated with increases in film conductivity. Valence-band spectra for the *a*-TiO_2 films exhibited a defect-state peak below the conduction-band minimum (CBM), and increases in the intensity of this peak correlated with increases in the Ti^{3+} concentration measured by EPR as well as with increases in film conductivity. The temperature dependent conduction data showed Arrhenius behavior at room temperature with an activation energy that decreased with decreasing temperature, suggesting that conduction did not occur primarily through either the valence or conduction bands. The data from all of the measurements are consistent with a Ti^{3+} defect-mediated transport mode involving a hopping mechanism with a defect density of 10^{19} cm^{-3}, a 0.83 wide defect-band centered 1.47 eV below the CBM, and a free-electron concentration of 10^{16} cm^{-3}. The data are consistent with substantial room-temperature anodic conductivity resulting from introduction of defect states during the ALD fabrication process as opposed charge transport intrinsically associated with the conduction band of TiO_2.

I. INTRODUCTION

Water oxidation to evolve O_2(g) is a key process in the (photo-)electrochemical production of carbon-neutral fuels. Semiconductors with band gaps, $\mathbf{E}_g$, that allow substantial absorption of sunlight ($\mathbf{E}_g < 2$ eV) typically corrode, either through dissolution or through the formation of an insoluble insulating surface oxide, when placed in contact with an aqueous electrolyte and poised at a potential sufficiently positive to drive the water-oxidation half-reaction.[1] Such corrosion has impeded the development of fully integrated solar fuels devices that involve immersion of semiconductors in an electrolyte,[2] and is especially rapid in the strongly acidic or strongly alkaline electrolytes that are compatible with efficient operation of electrochemical cells and with existing ion-exchange membranes.[3] Coating such semiconductors with films that combine transparent, conductive oxides with active catalysts for the oxygen-evolution reaction (OER) has been shown to extend the lifetime of semiconductor anodes in aqueous electrolytes from seconds to hours or months,[4-13] depending on the specific materials and test conditions.

Coatings of amorphous TiO_2 (*a*-TiO_2) supporting a Ni OER catalyst provide stability against corrosion of technologically important n-type semiconductors including n-Si, n-GaAs, and n-CdTe, in strongly alkaline electrolytes under water-oxidation conditions.[4, 14] The relative alignment between the valence-band maximum (VBM) of these n-type materials and the VBM of n-type TiO_2 ($\mathbf{E}_g \sim 3.3$ eV) predicts an ~ 2 eV barrier to the transport of holes from the smaller-band-gap material into the *a*-TiO_2.[15] Nevertheless, these heterojunction devices support high anodic current densities (> 100 mA cm^{-2}).[4, 14] Conduction through the *a*-TiO_2 films has been shown to be essentially independent of the film thickness, with high conductance observed for films as thick as 143 nm; however, the interfacial conductance is strongly dependent on the top

contact. Specifically, to drive anodic current densities of 50 – 120 mA cm^{-2}, an Ir top contact increased the voltage required by ~ 400 mV relative to devices with Ni top contacts.[4] X-ray photoelectron spectroscopic (XPS) data indicate a band alignment that produces rectifying behavior for *a*-TiO_2 interfaces with n-Si and n^+-Si surfaces, and an ohmic contact between *a*-TiO_2 and p^+-Si.[16] Ambient-pressure XPS (AP-XPS) data of p^+-Si|*a*-TiO_2 electrodes under potential control indicate that the addition of Ni to the surface of *a*-TiO_2 changes the electrical behavior of the *a*-TiO_2|liquid junction. Bare *a*-TiO_2 electrodes in contact with solution are 'rectifying' for the oxidation of water or $Fe(CN)_6^{4-}$. This rectifying behavior is also observed for contact between a Hg droplet and bare *a*-TiO_2. The addition of a Ni layer to the *a*-TiO_2 makes the junction ohmic, removing a large energetic barrier to conduction across the *a*-TiO_2.[17]

These data provide a detailed picture of the energetics at n-Si|*a*-TiO_2|Ni|1.0 M KOH(aq) interfaces. However, the mechanism of conduction across the n-Si|*a*-TiO_2|Ni junctions, despite the unfavorable band alignment energetics, remains to be elucidated. XPS valence-band data show a weak peak ~ 2 eV above the valence-band maximum, suggesting the possibility of defect-based transport.[4] However, subsequent studies have observed anodic conduction by TiO_2 films synthesized using various techniques, including crystalline films, and did not yield a dependence of conduction on defect states.[18] For TiO_2-coated photocathodes, conduction occurs via electron transport in the TiO_2 conduction band.[19-21] Such electron transport mediated by the conduction band has been hypothesized to be a generic mechanism applicable to photoanodes, with TiO_2 operating as an ohmic contact to the underlying n-type semiconductor, with electrons being transported from solution via the TiO_2 conduction band recombining with holes at the semiconductor|TiO_2 junction.[22]

Ti^{3+} states (observable by electron-paramagnetic resonance, EPR and XPS valence band spectra) play a large role in the conductivity, light absorption, and many other properties of TiO_2.[23-30] The mechanism of facile hole conduction through *a*-TiO_2, despite the 3.0 eV band gap and unfavorable band edge energetics for either electron or hole conduction from small band gap inorganic semiconductors has not yet been elucidated. A greater understanding of the transport mechanism would provide insight into the utility and mechanism underpinning the use of ALD *a*-TiO_2 as a protection layer for a wide variety of photoanodes.

We describe herein a detailed investigation of conduction across p^+-Si|*a*-TiO_2 junctions, including temperature-dependent DC conductivity, AC conductivity, space-charge-limited current spectroscopy, electron paramagnetic resonance (EPR) and X-ray photoelectron spectroscopy (XPS). The experiments were designed to elucidate the mechanism of anodic conduction in *a*-TiO_2 layers as well as the factors that control the observed conductivity as the metal contact to the *a*-TiO_2 layer is varied. We consequently have explored the role of defect states in conduction across *a*-TiO_2 films fabricated by a variety of methods, as well as the importance of the energy-band positions of the Si and the top contact relative to the TiO_2 band positions. We have moreover applied the information gained from these studies to aid in the design of stable Si|*a*-TiO_2 photoanodes with high fill factors for solar-driven water oxidation in contact with acidic aqueous electrolytes.

II. EXPERIMENTAL

A. Sample Preparation

Materials and Chemicals

Water with a resistivity, ρ, > 18 MΩ·cm was obtained from a Barnsted Millipore purification system and was used throughout. All chemicals, including sulfuric acid (99.999%,

Sigma-Aldrich and ~ 18 M, ACS Reagent Grade, J.T. Baker), hydrogen peroxide (~ 30%, ~ 13 M, VWR), hydrochloric acid (ACS Grade, VWR), and buffered HF (aq) (semiconductor-grade, Transene), were used as received, unless otherwise noted. Two types of crystalline, single-side polished, Si substrates were used: p^+-Si(100) (Boron-doped, $\rho < 0.002$ Ω·cm, Addison Engineering) and n-Si(100) (Phosphorus-doped, $\rho = 2 – 3$ Ω·cm, Addison Engineering).

Preparation of Substrates

The Si wafers were cleaned using an RCA SC-1 procedure that consisted of a 10 min soak in a 3:1 (by volume) solution made from 3 parts H_2SO_4 (aq) (~ 18 M) and 1 part H_2O_2(aq) (~ 13 M). The samples were then briefly etched in a solution of buffered HF(aq) (Transene). The Si samples were cleaned using an RCA SC-2 procedure by soaking the samples for 10 min at 75 °C in a 5:1:1 (by volume) solution of H_2O, HCl(aq) (~ 11 M), and H_2O_2(aq) (~ 13 M). The RCA SC-2 procedure left a thin passivating oxide layer on the Si surface.

Atomic-Layer Deposition (ALD) of TiO_2 Thin Films

TiO_2 films were grown using two different precursors, tetrakis(dimethylamido)-titanium (TDMAT), and $TiCl_4$. For TiO_2 films prepared from the TDMAT precursor, a Cambridge Nanotech S200 or Fiji F200 ALD system was used to deposit TiO_2 films onto Si wafers or onto Pyrex micro cover glass slides (VWR). The defect characteristics of TiO_2 were similar for films prepared from either reactor. Each ALD cycle consisted of a 0.10 s exposure to TDMAT (Sigma-Aldrich, 99.999%), a N_2(g) (Airgas, 99.999%) purge, a 0.015 s exposure to H_2O, and a final N_2(g) purge. Research grade 20 sccm N_2(g) was used for the N_2(g) purges, and each N_2(g) purge was 15 s in duration. During deposition, the substrate and the TDMAT precursor were heated to 150 °C and 75 °C, respectively, while the H_2O remained at room temperature. Most samples were prepared with 1500 cycles, giving a nominal thickness of 68 nm. The thickness was chosen

to be consistent with previous work. At this thickness, the *a*-TiO_2 minimizes the reflection as a single-layer anti-reflection coating while still providing facile electronic conduction and corrosion protection of the underlying photoanode.[31]

TiO_2 films from the $TiCl_4$ precursor were deposited onto p^+-Si substrates in a hot-wall, flow-tube reactor with custom-designed sequencing software.[32] The precursor-gas lines were maintained at 110 °C whereas the precursor was maintained at room temperature. Each ALD cycle consisted of a 0.20 s exposure to $TiCl_4$ (Strem, 99%), a 45 s N_2(g) purge, a 0.10 s exposure to H_2O, and a final 30 s N_2(g) purge and the N_2(g) flow rate was 150 sccm. Films were deposited to a predetermined thickness of ~ 60 nm at chamber temperatures of 50, 100, or 150 °C. The film thickness and refractive index were measured via spectroscopic ellipsometry (J.A. Woollam Co., alpha-SE) and were fit to a Cauchy model.

Electron-Beam Metal Deposition

Samples were patterned via optical lithography, mounted with double-sided carbon tape, and pumped down to a base pressure of $<10^{-5}$ Torr in an electron-beam evaporator system (Ångstrom Engineering Inc.). Ti, Mg, Ni, Au, Ir, Pt and Pd were evaporated from source metals that were at least 4N purity. Deposition rates ranged from 0.020 to 0.080 nm s^{-1}, as monitored by a quartz-crystal microbalance. Deposition was stopped when the film thickness exceeded ~ 35 nm.

Electrode Fabrication

Electrodes were fabricated by using a scribe to cleave the e-beam deposited samples into ~ 0.1 cm^2 pieces. The samples were patterned into isolated pads for solid-state measurements or into islands for electrochemical measurements. A positive photoresist, S1813 (Shipley), was patterned, metal pads or islands deposited, and then the photoresist was removed by gently

sonicating in acetone for ~ 1 min to leave the desired pattern. Ohmic contact was made by scratching the back of the p^+-Si or n-Si sample with an In-Ga eutectic (Alfa-Aesar, 99.999%), and the back contact to the sample was affixed to a Cu wire with double-sided Cu tape. The Cu wire was threaded through a glass tube (Corning Incorporation, Pyrex tubing, 7740 glass), and all but the front of the sample was encapsulated with Loctite epoxy (Hysol 9462). After curing overnight, the electrode was scanned with an Epson scanner (V370) and analyzed with ImageJ software, to determine the area of the exposed region, which was ~ 0.1 cm^{-2}.

B. Conductivity Measurements

Current density versus voltage (*J-V*) data were collected on solid-state samples that had various combinations of metal contacts on degenerately boron-doped p^+-Si substrates coated with the *a*-TiO_2. The electrical data were collected using a Bio-Logic SP-200 potentiostat in a two-electrode setup with the working electrode lead connected to the bottom contact (Si back-side) and the counter and reference electrode leads connected to the top contact (metal pad). For electrical contact, In-Ga eutectic was scratched onto the back of the Si as well as onto the top side of the double-sided Cu tape that had been affixed to a glass slide for structural support. *J-V* data were collected at 100 mV s^{-1}, starting at an applied bias of 0 V versus the counter electrode.

Temperature-Dependent Conductivity

The substrates for the measurements were p^+-Si wafers coated with 1500 cycles (~ 68 nm) of ALD *a*-TiO_2 that was then patterned with Ni islands. During the variable temperature measurement, the samples were loaded into a Janis CCS-100/204N cryostat, and *J-V* data were obtained from 10 to 310 K using an Agilent B1500A semiconductor-device analyzer with medium-power source-measurement modules as well as atto-sense and switch units for high-

resolution current sensing. The conductivity was obtained by fitting the measured resistance data to a computational model using the AC/DC module in COMSOL Multiphysics software.

For resistance measurements from 180 K to 300 K, the samples were loaded into another cryostat. In both temperature-dependent measurements, the temperature of the sample was controlled using a Lake Shore auto-tuning temperature controller with a Si diode temperature sensor placed in thermal contact with the sample.

Potential-Dependent Conductance Measurements on Electrochemical Field-Effect Transistors (EC-FET)

The conductance of *a*-TiO_2 films in contact with an electrolyte solution was measured with interdigitated electrodes (IDE) in an electrochemical field-effect-transistor configuration (EC-FET).[33-34] The substrates for the measurements were clean glass microscope slides that had been lithographically patterned with 224 interdigitated Ti fingers of 20 μm × 2 mm × 100 nm (width × length × thickness). Alternate fingers were spaced 20 μm apart from one another. The substrate had 1500 cycles (~ 68 nm) of *a*-TiO_2 deposited via ALD. The front contacts were kept free of deposited material by use of a glass slide as a physical mask. The conductance of the *a*-TiO_2 in contact with 1.0 M H_2SO_4(aq) was measured using a BioLogic SP-300 bipotentiostat that allowed control of the potential of each electrode (channels) of the IDE array independently with respect to the reference electrode in the solution. Both channels were set to the desired gate potential (V_{gate}), and the capacitance current was allowed to decay for 30 s, to establish the electron occupancy in the film and to set the potential of the film relative to the reference potential. The potential of channel 2 was then offset by ± 25 mV with respect to channel 1, and the source-drain potential (V_{SD}) was varied in 10 mV increments. Under the conditions investigated, the source-drain current (I_{SD}) was proportional to V_{SD}, allowing an estimate of the

film conductance as a function of V_{gate}. V_{gate} was varied across the potential range between the onset of accumulation and deep depletion. The film conductivity was calculated using an IDE cell constant, K_{IDE}, of 0.045 cm^{-1}, which was estimated from the geometry of the IDE[35] using eq 1:

$$K_{ide} = \frac{2\left(s/w\right)^{\frac{1}{3}}}{l\left(n-1\right)} \quad (1)$$

where s is the spacing between the electrode digits (20 μm), w is the width of the electrode (20 μm), l is the length (2 mm), and n is the number of digits (224). This process produced a cell constant of K_{ide} = 0.045 cm^{-1}. The measured conductance, G_{ecfet}, was converted to units of conductivity by use of eq 2:

$$\sigma_{ecfet} = K_{ide} G_{ecfet} \quad (2)$$

C. Physical Characterization of *a*-TiO_2

Electron Paramagnetic Resonance Spectroscopy

Electron paramagnetic resonance (EPR) spectra were collected at 77 K using a Bruker EMX X-band continuous-wave spectrometer. Data were collected for samples in liquid N_2 in a finger Dewar. Samples were prepared by depositing 1500 ALD cycles of *a*-TiO_2 onto VWR micro-cover glass slides (0.15 ± 0. 02 micron thick). The slides were then diced into 2×2 mm^2 pieces using a Dynatex GST-150 scriber-breaker. The diced samples were then placed in EPR tubes.

Due to sample variations, all of the TiO_2 (50 °C, 100 °C, 150 °C $TiCl_4$ and TDMAT) films were of slightly different thickness as measured by ellispometry. To ensure a uniform amount of TiO_2 was maintained between samples, the total area was varied. For instance, if the TDMAT

and 50 ºC $TiCl_4$ TiO_2 had a thickness of 68 and 62 nm, respectively, then the area ratio of TDMAT:50 ºC $TiCl_4$ TiO_2 was adjusted to 1.0:1.1, to ensure an equivalent amount of TiO_2.

Photoelectron Spectroscopy

X-ray photoelectron spectroscopic (XPS) data were collected on ALD-deposited *a*-TiO_2 on p^+-Si using a Kratos Axis Ultra system with a base pressure of 1×10^{-9} Torr. The x-ray source was a monochromatic Al Kα line at 1486.6 eV. Photoelectrons were collected at 0° from the surface normal with a retarding pass energy of 160 eV for survey XPS scans, 10 eV for high-resolution core levels, and 20 eV for valence-band XPS scans.

Work function measurements were performed using He I ultraviolet photoelectron spectroscopy (UPS) on the Kratos Axis Ultra system. A pass energy of 5 eV was used in conjunction with an aperture of 110 μm. Prior to the measurements, pure metal samples (>99.99%) were sputter cleaned for 30 min with 4 kV Argon Ions. The work function (ϕ_{WF}) was calculated from the measured spectra on a kinetic energy scale using eq (3):

$$\phi_{WF} = E_{sec,meas} - E_{F,\,meas} + 21.21 \qquad (3)$$

where $E_{sec,\,meas}$ and $E_{F,\,meas}$ are the measured energy of the secondary electron cutoff and the Fermi energy, respectively, and 21.21eV is the photon energy for He I excitation. The secondary electron cutoff and Fermi energy were obtained by calculating the intercept of a linear fit of the steep electron cutoff to that of the background and by fitting a Fermi distribution to the valance-band maximum, respectively.

Secondary-Ion Mass Spectroscopy

Secondary-ion mass spectroscopy (SIMS) data were collected on a Cameca SIMS-7f GEO. A 100 μm × 100 μm area of the sample surface was ionized and sputtered by a 7 keV Cs^+ primary ion beam with no substrate biasing. A mass spectrometer collected and analyzed the

ejected secondary ions. The count rates of ^{30}Si, ^{48}Ti, $^{12}C + ^{133}Cs$ and $^{14}N + ^{133}Cs$ were collected as a function of sputtering cycle. SIMS data were collected for all TDMAT and $TiCl_4$ *a*-TiO_2 films.

Attenuated Total Reflection Infrared Spectroscopy

Attenuated Total Reflection Infrared Spectroscopy (ATR-IR) spectra were collected using a Thermo Scientific Nicolet 6700 optical spectrometer equipped with thermoelectrically cooled deuterated L-alanine-doped triglycine sulfate (DLaTGS) detector, electronically temperature-controlled (ETC) EverGlo mid-IR source, N_2(g) purge, KBr beam splitter, and diamond ATR crystal single-reflection Smart-iTR accessory. After data collection, spectra for ALD films on glass substrate were corrected using pristine glass as the background. Air was used as background for ALD films deposited on silicon substrate. In addition, the baseline was flattened when needed. TIRS data collection and processing was performed using OMNIC software v.9.2.41.

D. Electrochemical Characterization

Electrochemical data were obtained using a BioLogic SP-200 potentiostat in a three-electrode configuration with 1.0 M H_2SO_4(aq) as the electrolyte. A carbon rod (Strem Chemicals, 99.999%) was used as the counter electrode, and a $Hg/HgSO_4$ electrode (Gamry Instruments) was used as the reference electrode. An ELH-type tungsten-halogen lamp provided light that passed through a quartz diffuser to reach the Pyrex electrochemical cell. The illumination intensity was measured by a Si photodiode (Thorlabs) and the light intensity was adjusted to produce the same current on the photodiode as was produced by illumination with 100 mW cm^{-2} of Air Mass 1.5 sunlight. Cyclic voltammetric data were collected at a 40 mV s^{-1} scan rate.

III. Results

A. Work Functions of the Metals

Figure S1 shows representative work function measurements by UPS for Ni, Pd, Pt, Ir and Au. The spectra allowed determination of the work functions for these polycrystalline metals (purity >99.99 %) as: 5.09 ± 0.4, 5.27 ± 0.2, 5.56 ± 0.07, 5.32 ± 0.2, and 5.05 ± 0.3 eV for Ni, Pd, Pt, Ir, and Au, respectively. These work function values are in good agreement prior work function measurements on polycrystalline metals.[36-38] The work functions of Mg and Ti were taken to be 3.66 ± 0.2, and 4.33 ± 0.2 eV, respectively.[36]

B. Conductivity of p^+-Si|*a*-TiO_2|metal Devices

J-V Characteristics of p^+-Si|a-TiO_2|metal Devices

Figure 1 shows representative solid-state *J-V* characteristics for p^+-Si|*a*-TiO_2|metal devices with *a*-TiO_2 grown on the p^+-Si substrates via 1500 ALD cycles using a TDMAT precursor and substrate temperature of 150 °C. The ALD procedure yielded ~ 68 nm thick *a*-TiO_2 films. The *J-V* characteristics showed ohmic (linear) behavior at biases < 50 mV. **Figure S2** shows the normalized differential conductance as a function of applied bias for a p^+-Si|*a*-TiO_2|Ni device, which is consistent with behavior typical of dielectric films.[39 40]

The current density passed as a function of applied bias depended on the top contact, **Figure 1**, with devices having Ti, Mg or Ni top contacts behaving almost mutually identically, especially at low biases. At the same applied bias, devices with Au, Ir, Pt or Pd top contacts passed ⩽ 10% of the current densities of devices having Ti, Mg or Ni as a top contact. For example, at an applied bias of 0.1 V, devices with Ti, Mg, or Ni top contacts passed current densities of ~ 60 mA cm^{-2}, as compared to the current densities passed by devices with Au (8.7 mA cm^{-2}), Ir (5.5 mA cm^{-2}), Pt (3.6 mA cm^{-2}), or Pd (1.5 mA cm^{-2}) contacts. Compared to

devices with Ti, Mg or Ni top contacts, the devices with Au, Ir, Pt or Pd top contacts required an additional 90 – 250 mV of bias to pass current densities of 10 mA cm^{-2}, as well as an additional 150 – 330 mV of bias to pass current densities of 30 mA cm^{-2}. The conductivities at low applied biases (< 50 mV) were determined from linear fits of the data (**Figure 1**). The contact resistances were determined by transmission line measurements, and the compensated voltages between different metal contacts were measured for all devices (**Table S1**). Although the contact resistance increased as the work function of the metal increased, the metals with the higher work functions yielded sufficiently low current densities that the total voltage compensation would not create a noticeable change in the *J*-*V* behavior over the measurement range depicted in **Figure 1**.

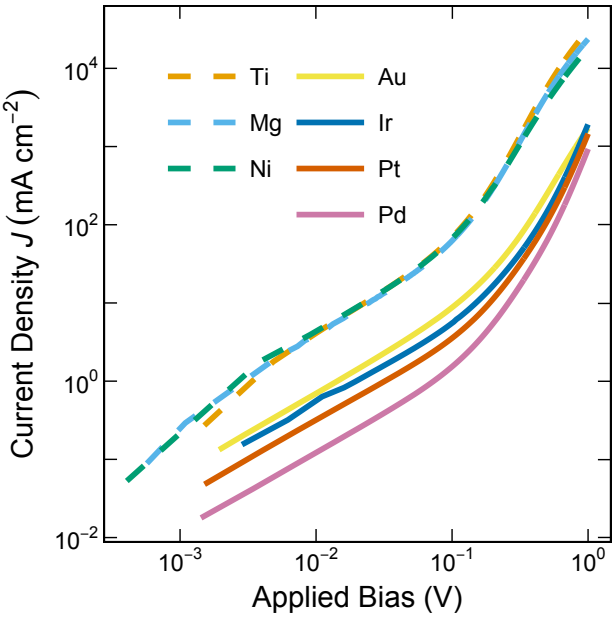

Figure 1. Current density (*J*) vs applied bias (*V*) for solid-state p^+-Si|*a*-TiO_2|metal devices. The *a*-TiO_2 was ~ 68 nm thick. The devices were tested in a two-electrode configuration, and the bias was applied across the device using the p^+-Si side as the working electrode and the metal side as the counter electrode.

Table 1. Conductivities for the devices with varied metal contacts as determined from a fit of the *J-V* behavior in the low-bias regions. At least 5 samples with each metal were tested, and error estimates represent one standard deviation.

Top Contact	Conductivity (S cm^{-1})	Work Function (eV)
Ti	$(85 \pm 18) \times 10^{-5}$	4.33 ± 0.20
Mg	$(85 \pm 1.2) \times 10^{-5}$	3.66 ± 0.20
Ni	$(95 \pm 4.0) \times 10^{-5}$	5.09 ± 0.39
Au	$(13 \pm 1.7) \times 10^{-5}$	5.05 ± 0.30
Ir	$(4.0 \pm 1.6) \times 10^{-5}$	5.32 ± 0.18
Pt	$(8.3 \pm 1.8) \times 10^{-5}$	5.56 ± 0.07
Pd	$(2.3 \pm 0.45) \times 10^{-5}$	5.27 ± 0.18

Space-Charge-Limited Current (SCLC) Spectroscopy

Figure 2a shows a plot of the *J-V* characteristics for a p^+-Si|*a*-TiO_2|Pt device, extended to 5 V of applied bias. At ~ 5 V, the current increased abruptly, consistent with a space-charge limited current in the trap-free regime.[41-44] Similarly extended *J-V* characteristics can be seen in **Figure S3** for devices with Au, Ir or Pd contacts. The number of traps, the majority charge-carrier mobility, and the charge-carrier concentration were calculated from the threshold voltages for trap filling, the *J-V* behavior in the trap-free regime, and the *J-V* behavior in the ohmic regime, respectively, according to eqs 4–6:[41-44]

$$V_{TF} = \frac{qN_T L^2}{\varepsilon_0 \varepsilon} \quad (4)$$

$$J_{TF} = \frac{9\varepsilon\mu V^2}{8L^3} \quad (5)$$

$$J_{\Omega} = \frac{qn\mu V}{L} \quad (6)$$

where V_{TF} is the threshold voltage for trap filling, J_{TF} is the current density in the trap-free region, J_{Ω} is the current density in the ohmic region, q is the absolute charge of an electron, N_T is the trap density, L is the thickness of the sample, ε_0 is the permittivity of free space, ε (= 112) is the dielectric constant of TiO_2, μ is the mobility of the majority carriers, and n is the mobile charge-carrier density. The calculated trap densities, mobilities, and effective mobile charge-carrier densities for p^+-Si|*a*-TiO_2|metal devices with various metal top contacts are tabulated in **Table S2**.

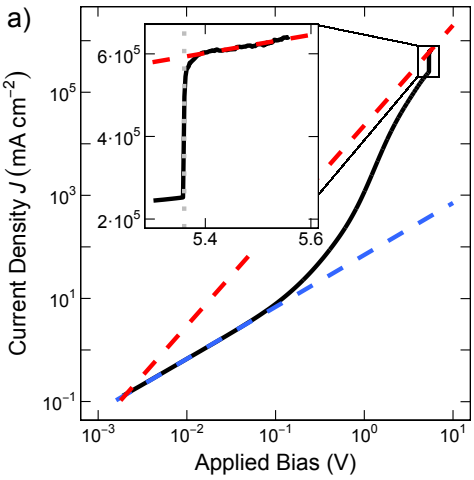

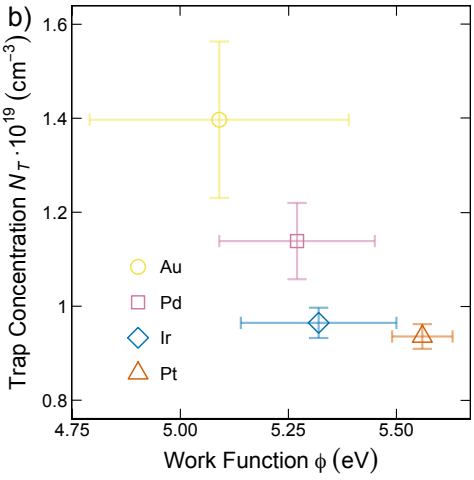

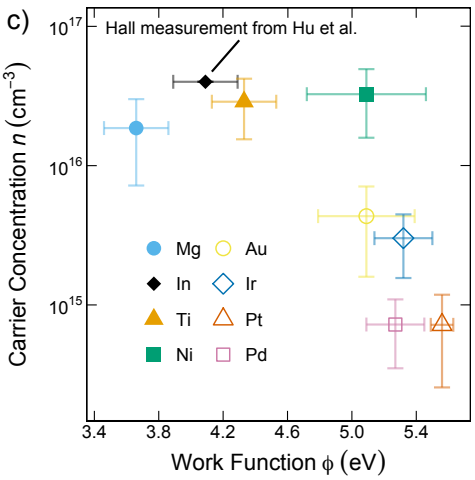

Figure 2. a) *J-V* characteristics of a solid-state p^+-Si|*a*-TiO_2|Pt device, extended to applied biases > 5 V. The *a*-TiO_2 was ~ 68 nm thick. The inset is a plot of the crossover into the trap-filled regime. Linear regressions are shown for the ohmic region at low bias (blue dashed line), and the trap-filled space-charge-limited regimes (red dashed line in the inset). b) Concentration of trap states for devices with top contacts to high-work-function metals. c) Calculated free-carrier concentrations for varied metal top contacts.

Figure 2b shows the dependence of the number of traps measured by SCLC spectroscopy on the work function of the top contact used for the p^+-Si|*a*-TiO_2|metal device.[36, 45-46] The number of traps measured by SCLC decreased only slightly as the work function of the top contact increased. For low-work-function metals, the trap concentration could not be measured before the voltage limits of the potentiostat were reached, implying trap densities > 1.5×10^{19} cm^{-3}.

Figure 2c shows the variation of the calculated free-carrier concentration for each metal contact as a function of the work function of each metal. The free-carrier concentration was calculated by using the value of the mobility found in the trap-free regime (eq 5) with a Pt contact ($6.5 \pm 3 \times 10^{-4}$ cm^2 V^{-1} s^{-1}), in conjunction with the slopes of the ohmic regions for the various top contacts, according to eq 6. Below a work function of ~ 5.2 eV, the (averaged) carrier concentration was essentially independent of the work function of the top metal contact,

whereas for a work function > 5.2 eV, the (averaged) free-carrier concentration becomes dependent on the work function and thus decreased by $10^1 - 10^2$ cm^{-3}. Although the mobility is not a constant for different dopant concentrations, the mobility was approximated to be independent of the free-carrier concentrations. This approximation is in agreement with the free-carrier density measured previously by Hall measurements with In contacts (**Figure 2c**).[4] In addition, the mobility measured is in agreement with the predicted mobility of 2×10^{-4} cm^2 V^{-1} s^{-1} by Pham et al using DFT+U methods.[47]

AC Conductivity

Figure 3 shows the AC conductivity as a function of frequency for a p^+-Si|*a*-TiO_2|Ni device at room temperature and under an applied bias of 300 mV. The conductivity of the sample was 3.0×10^{-6} S cm^{-1} for frequencies $\leqslant 10^5$ Hz, and increased exponentially at frequencies > 1×10^4 Hz.

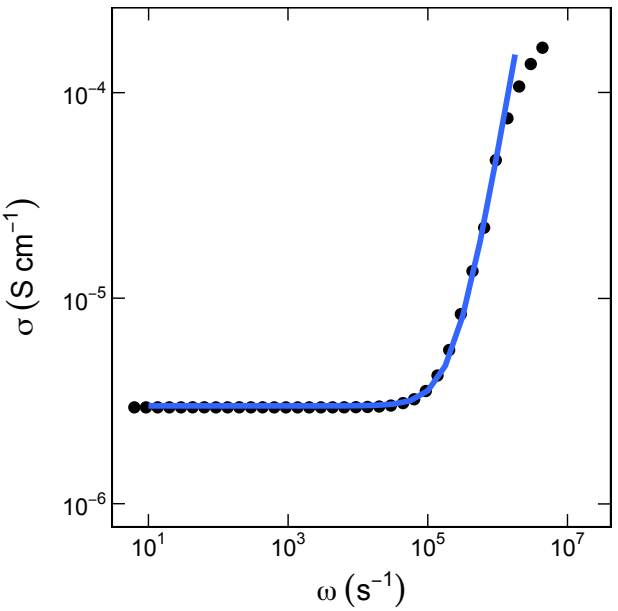

Figure 3. AC conductivity of a solid-state p^+-Si|*a*-TiO_2|Ni device measured in a two-electrode configuration with a bias of 300 mV applied between the p^+-Si side and the Ni side of the device. The blue line shows a fit of the frequency-dependent region of the data to a power-law model,

$\sigma(\omega) = \sigma_{DC} + A\omega^{S}$, where $\sigma_{DC} = 9.9 \times 10^{-17}$ S m^{-1}, $A = 2.96 \times 10^{-6}$ S m^{-1}, and $s = 1.95$.

Temperature-Dependent Conductivity of Ni|a-TiO$_2$|Ni Devices

Figure 4 shows the conductivity as a function of temperature for a Ni|*a*-TiO$_2$|Ni through-layer device in which the thickness of the *a*-TiO$_2$ layer was 68 nm, measured at temperatures between 10 K and 310 K. The data showed two regions, each with an Arrhenius-type exponential temperature dependence. Activation energies for charge transport were calculated from the slopes of the linear fits. The model yielded an activation energy for charge transport at temperatures in the 250 – 310 K range of 350 ± 15 meV, which is substantially larger than the ~ 7 meV activation energy calculated for charge transport at temperatures in the 100 – 125 K range. The activation energy continuously decreased as the temperature decreased.

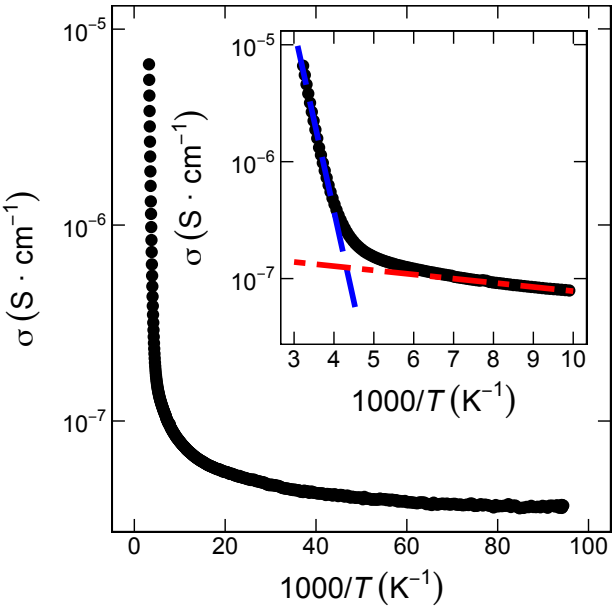

Figure 4. Temperature-dependent conductivity of a Ni|*a*-TiO$_2$|Ni device in which the thickness of the *a*-TiO$_2$ layer was 68 nm. The inset shows the same data for the 100 – 310 K temperature range; the blue and red dashed lines are linear fits of the data for temperatures in the range of 250 – 310 K, and 100 –125 K ranges, respectively.

Potential-Dependent Conductivity of a-TiO$_2$

Figure 5 shows the dependence of the conductivity on the gate potential (V_{gate}) for an *a*-TiO_2 film with Ti contacts in the EC-FET configuration in contact with 1.0 M H_2SO_4(aq), which allowed the conductivity of the TiO_2 to be measured as a function of the potential, or Fermi level, of the gate electrode. V_{gate} was referenced against a reversible hydrogen electrode (RHE) and was varied across a potential range relevant to water splitting (-0.4 to +1.75 V versus RHE). The data showed a sharp increase in conductivity as V_{gate} became more negative than -0.3 V versus RHE, indicating a sharp increase in electron transport in the conduction band. At these potentials the TiO_2 is in accumulation. At more positive potentials, the conductivity showed a weak dependence on V_{gate}, and decreased by ~ 1% over a range of 2 V. These data suggest the presence of a finite density of states at potentials extending for >2 eV below the TiO_2 conduction-band edge. These results generally agree with data for Si|*a*-TiO_2 and Si|*a*-TiO_2|Ni samples observed under electrochemical conditions in 1.0 M KOH(aq). The Si|*a*-TiO_2 showed a flat-band potential of -0.9 vs Ag/AgCl, i.e. +0.1 V versus RHE, whereas the Si|*a*-TiO_2|Ni sample showed Fermi-level pinning over a broad potential range (0 to 1.4 V versus RHE).[17, 48]

The conductivity measured for *a*-TiO_2 using the IDE in 1.0 M H_2SO_4(aq) was $1.17 \pm 0.45 \times 10^{-5}$ S cm^{-1}, with three samples measured (**Table S3**). Measurements made in air using one of the IDEs used in the EC-FET experiments showed a dry conductivity equal to that for the electrode in contact with the electrolyte, suggesting that the IDE electrode was unaffected by immersion in the electrolyte, and indicating negligible electrolyte-induced effects on the conductivity.

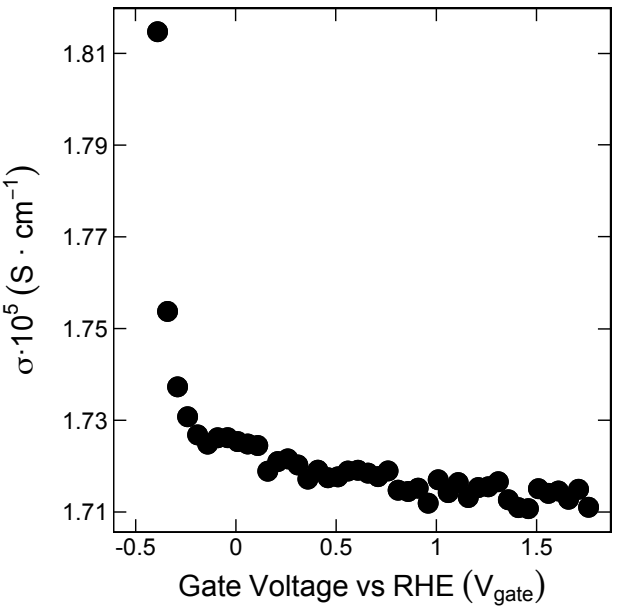

Figure 5. Conductivity of *a*-TiO_2 as a function of the gate voltage (V_{gate}) applied to interdigitated contacts covered by 1500 cycles (approximately 68 nm) of *a*-TiO_2.

C. Effects of ALD Process on Physical Characteristics of ALD *a*-TiO_2

J-V Characteristics of p^+-Si|a-TiO_2|Ni Devices

Figure 6 shows the *J-V* characteristics of p^+-Si|*a*-TiO_2|Ni devices, with the *a*-TiO_2 films prepared via ALD using either a TDMAT precursor with the substrate held at 150 ºC or a $TiCl_4$ precursor with the substrate held at 50, 100 or 150 °C. Films deposited from TDMAT at 150 °C or from $TiCl_4$ at 50 or 100 °C had undetectable levels of crystallinity, whereas small fractions of crystallinity were detected from films prepared at 150 °C, as measured by Raman spectroscopy (**Figure S4a**) and glancing incidence X-ray diffraction (**Figure S4b**).[49-50] In addition, the main phase of the films were probed by FTIR. No evidence was found to support the presence of H_2TiO_3 in the films deposited on glass (**Figure S5a)** and Si (**Figure S5b**).

All of the TiO_2 devices exhibited ohmic regions at low biases, however for the same applied bias, the TDMAT-TiO_2 film passed a more than an order of magnitude higher current

density than the least resistive $TiCl_4$-TiO_2 film. The conductivities of the $TiCl_4$-TiO_2 films increased with growth temperature. The mobilities of the various TiO_2 films were calculated according to eq 5, and the free-carrier concentrations were calculated using eq 6. The free-carrier concentrations for the $TiCl_4$-TiO_2 films were smaller by one to three orders of magnitude than that of the TDMAT film.

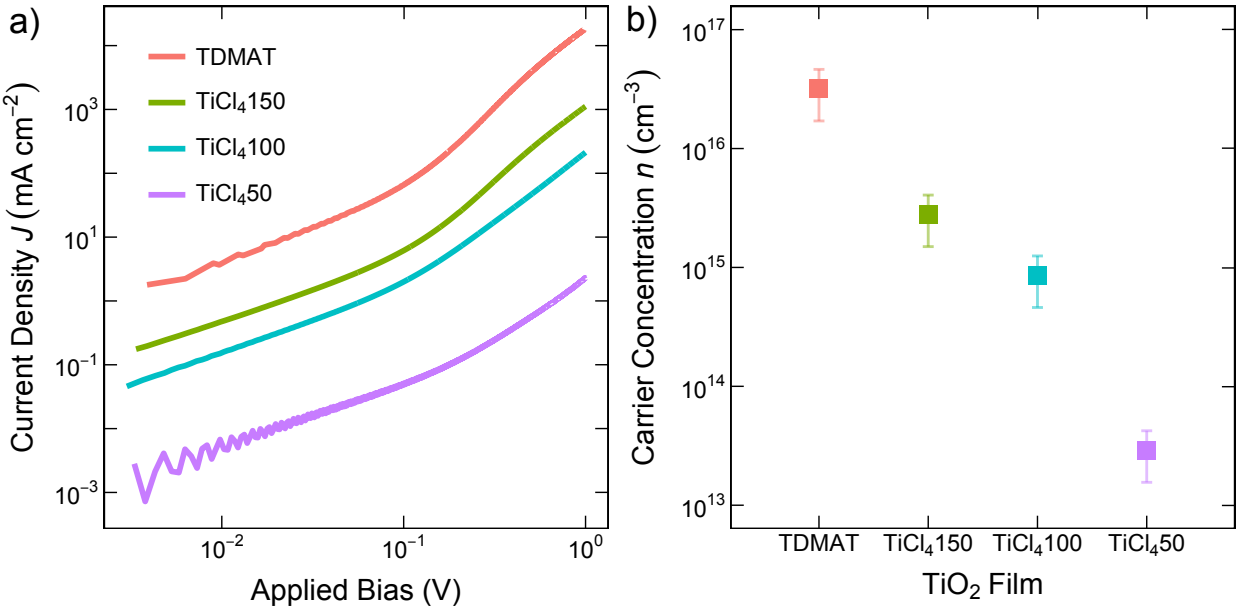

Figure 6. a) *J-V* characteristics and b) free-carrier concentrations calculated for various TiO_2 films grown on p^+-Si substrates and contacted with Ni. The film grown from TDMAT at 150 °C was ~ 68 nm thick; the films grown from $TiCl_4$ were ~ 60 nm thick and were grown at varied temperatures of 50, 100, or 150 °C.

Valence-Band Spectra

Figure 7a shows the XPS valence-band spectra for an *a*-TiO_2 film prepared by ALD using a TDMAT precursor at 150 °C. The observed signal was in accord with previously reported valence-band spectra of identically prepared *a*-TiO_2.[4, 18] After a Shirley background was subtracted, the spectra showed a peak centered at 1.07 ± 0.07 eV with a full width a half maximum, FWHM, of 0.83 eV. Using the previously determined position of the Fermi level in

TiO_2 as 0.40 eV below the CBM, the defect band was centered at 1.47 eV and extended from ~ 1 – 1.9 V below the CBM, i.e. from ~ 0.6 – 1.5 eV below the Fermi level.[16] Previous analysis has located the center of the defect band at ~ 1.34 eV below the CBM, with a FWHM of 0.83 eV, consistent with the results described herein.[16]

Figure 7b presents the valence-band spectra of ALD-TiO_2 films prepared using different precursors and growth temperatures. All of the valence-band spectra showed a peak at 1.07 ± 0.07 eV, with mutually similar FWHMs. The TDMAT-TiO_2 film exhibited the largest valence-band signal, while the $TiCl_4$-TiO_2 films exhibited weaker signals that increased with growth temperature. The relative peak intensities (normalized to the largest signal) were 0.62 ± 0.2, 0.69 ± 0.2, 0.71 ± 0.3 and 1 ± 0.6, for the $TiCl_4$-TiO_2 films grown at 50 °C, 100 °C, 150 °C, and TDMAT-TiO_2, respectively. The averaged spectra and respective standard deviation can be seen in **Figure S6.**

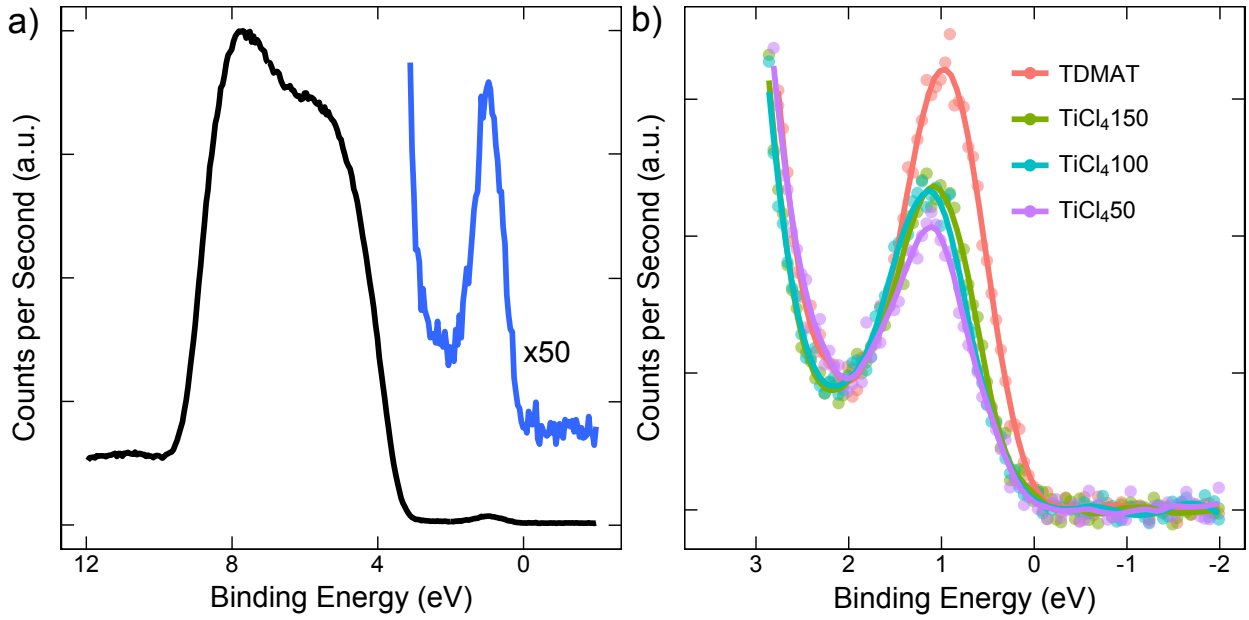

Figure 7. a) X-ray photoemission spectra (without background subtraction) for the valence band of *a*-TiO_2 grown via ALD using a TDMAT precursor at 150 °C. b) Comparison of the X-ray photoemission valence-band spectra of ALD *a*-TiO_2 films grown using a TDMAT precursor at

150 °C, or a $TiCl_4$ precursor at 50 °C, 100 °C or 150 °C.

Electron Paramagnetic Resonance Spectroscopy

Figure 8 compares the EPR spectra for the various ALD-TiO_2 films. The isotropic g-values extracted from the spectra were 1.939 and 2.000. The broad signal at 1.939 is consistent with the presence of Ti^{3+} since the signal is within the range of previously reported g-values, g = 1.92 to 2.00, for Ti^{3+} sites.[30, 51-55] The TDMAT-TiO_2 films exhibited a substantially larger Ti^{3+} signal than the $TiCl_4$-TiO_2 films. The $TiCl_4$-TiO_2 films grown at 150 °C and 100 °C exhibited a detectible signal for Ti^{3+}, while the $TiCl_4$-TiO_2 grown at 50°C showed no appreciable Ti^{3+} signal.

The signal at 2.000 observed in the spectra for 150 °C $TiCl_4$-TiO_2 film is attributable to either the variations of impurities within the glass substrate or electrons trapped at oxygen vacancy sites.[26, 56] The sharpness of the signal as well as appearance at g-values greater than the broad Ti^{3+} signal is consistent with the electrons trapped at oxygen vacancy sites. Additional control experiments showed that only a decrease in the signal at this g-value was observed with the substrate-only and EPR silent Al_2O_3 signal, as can be seen in **Figure S7a**. The same decrease was present in all other TiO_2 films but was not observed in the background (cavity-only) signal, which had no prominent features.

In addition, EPR measurements were performed at various angles of rotation. No shift was observed when the TDMAT *a*-TiO_2 sample was rotated within the EPR instrument. This result is expected as *a*-TiO_2 samples have an amorphous structure and the samples are macroscopically arranged randomly in the EPR tube. The results of the control experiments are presented in **Figure S7b**.

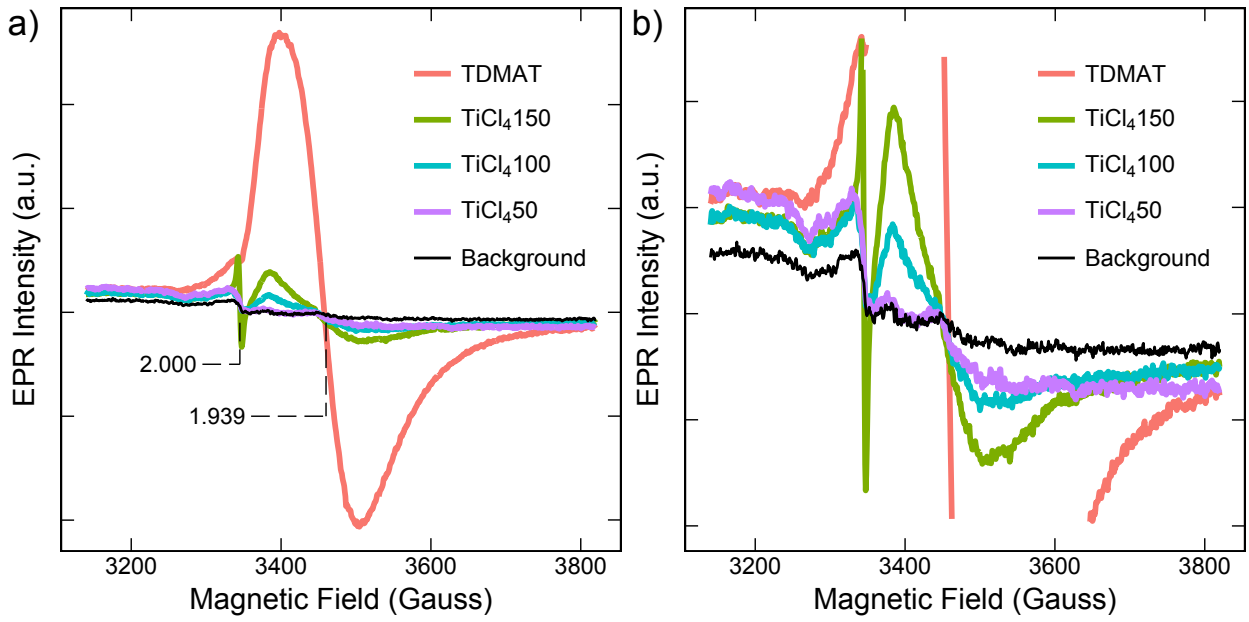

Figure 8. a) Electron paramagnetic resonance (EPR) spectroscopy for *a*-TiO_2 films grown via ALD using a TDMAT precursor at 150 °C, or a $TiCl_4$ precursor at 50 °C, 100 °C or 150 °C. b) EPR spectra rescaled to show the detail of the smaller peaks. The background spectrum includes the EPR tube and the glass substrate.

D. Application to Photoelectrochemical Water Oxidation in Acidic Aqueous Electrolytes

Figure 9 shows the voltammetric behavior of non-photoactive p^+-Si|*a*-TiO_2|Ir anodes and n-Si|*a*-TiO_2|Ir photoanodes under 1 Sun illumination in 1.0 M H_2SO_4(aq). The Ir was deposited on the *a*-TiO_2 as catalytic islands 3 μm in diameter on a 7 μm pitch. The Ir islands were 35 nm thick, and were deposited either directly on the *a*-TiO_2 or onto 35 nm of Ti on the *a*-TiO_2. Ti was selected as an intermediate contact because p^+Si|*a*-TiO_2 devices with Ti contacts had exhibited high conduction relative to devices with Ir contacts. The samples with the Ti interconnect performed substantially better than those without the Ti interconnect, as evidenced by a reduction in the overpotential required to reach 10 mA cm^{-2} of current density of 280 mV for the Ti|Ir n-Si devices and of 460 mV for the Ti|Ir p^+-Si devices.

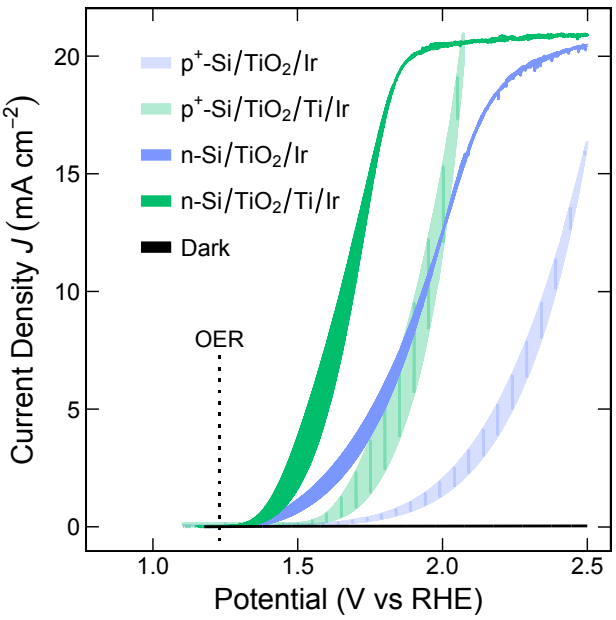

Figure 9. Cyclic voltammetry of non-photoactive p^+-Si|*a*-TiO_2 anodes and n-Si|*a*-TiO_2 photoanodes in contact with 1.0 M H_2SO_4. The samples were p^+-Si and n-Si substrates coated with 1500 ALD cycles of *a*-TiO_2 onto which metal-island top contacts were deposited. The metal top contacts to the *a*-TiO_2 layer were 35 nm thick islands of Ir, 3 μm in diameter pitched 7 μm apart, deposited either directly on the *a*-TiO_2 or onto a 35 nm thick Ti island interconnect. The CV sweep was conducted in the dark and 1 sun illumination for p^+-Si and n-Si, respectively, from 1.1 V vs RHE to 2.5 V vs RHE at scan rate of 40 mV s^{-1}.

IV. Discussion

A. Identity and Position of Defect States in ALD *a*-TiO_2

The valence-band spectra for *a*-TiO_2 deposited via ALD showed a small peak within the band gap of the TiO_2, centered at 0.94 eV below the Fermi level.[18, 39] The band had a FWHM of 0.83 eV, indicating that a wide energy band exists within the band gap. Defect bands in TiO_2 have been observed both for amorphous films grown by ALD as well as crystalline films grown by various methods.[57-63] The bands have been associated with oxygen and/or other defects on the surface of the TiO_2. Oxygen vacancy sites are often implicated and have been observed by TEM.[58] The defect band has been correlated with the introduction of imperfections into the crystal. [47, 64] Oxygen vacancies would provide doping and produce Ti^{3+} sites by the trapping of free electrons into localized Ti–O octahedra with an oxygen vacancy.[65] Theoretical calculations

favor oxygen vacancies as the structural origin of the defect sites, and calculations moreover have been used to calculate conduction by small polaron hopping.[47, 66-69]

Oxygen defects and Ti^{3+} sites dominate the physical and chemical properties in TiO_2.[47, 63-65, 67, 70-73] The bulk structure of reduced crystalline TiO_{2-x} contains defects of doubly charged oxygen vacancies, interstitial titanium defects, and other defects.[74] The defects vary with the amount of the oxygen deficiency[23] and vacancies on the surface have been imaged by scanning tunneling microscopy.[74-75] The number of vacancies can be controlled by the method of annealing, and surface vacancies can be healed by dosing with oxygen.[23] Additionally, self-doping of TiO_2 from oxygen vacancies yields Ti^{3+} sites.[28]

ALD TiO_2 grown at substrate temperatures < 300 ºC has been shown to be amorphous when annealed below 350 ºC but becomes crystalline when annealed above 350 ºC.[76-77] XPS studies of ALD *a*-TiO_2 have observed both a Ti^{3+} shoulder on the Ti 2p core level, and a small shoulder on the O1s spectra that is assigned to -OH groups on the surface.[61-62] Both normal and resonant valence band spectra show a peak at ~ 1 eV below the Fermi level that is due to titanium and attributable to Ti^{3+} states. The band is much weaker in crystalline TiO_2.[62]

XPS depth profiling was forgone because the Ti 2p XPS spectrum is heavily altered after Ar ion bombardment. Oxygen is preferentially removed thus reducing the TiO_2. The reduced states observed in the spectrum generated from the Ar ion bombardment are thus not an accurate representation of the underlying composition of the TiO_2.[78]. Instead we focused on angle dependent XPS spectroscopy where with increased electron emission angle Θ to the surface normal the inelastic mean free path for electrons is reduced. The values for Al Kα radiation are given in **Table S4**.

The concentration of the defect states (and Ti^{3+} states) has been investigated by angle dependent XPS.[17] No change in Ti 2p core level and defect band were detected. However, with increasing surface sensitivity a shoulder at 532.5 eV at the O 1s core level (attributed to dumbbell di-oxygen species, OH-groups and/or to reconstruction of the $TiO_{2)}$ was visible which increased in intensity with increased Θ. Here, we performed scans for Θ=0 and 70 with improved signal to noise ratio which are shown in **Figure S8**. Again, no difference between bulk or surface sensitive spectra could be observed indicating no surface re-oxidation of the defect band.

EPR spectra provided direct evidence of Ti^{3+} within the bulk *a*-TiO_2 films (**Figure 8**). The correlation between the strength of the Ti^{3+} signals in the EPR spectra and the strength of the defect-band peaks in the XPS valence-band spectra supports the assignment of the defect peak in the XPS valence-band spectra to localized Ti^{3+} sites. The films are amorphous, so the Ti^{3+} sites can be expected to show a dispersion in energy due to differences in Ti–Ti and Ti–O bond lengths,[79] consistent with the wide peak (FWHM = 0.83 eV) observed for the defect band.

The Ti^{3+} sites in the ALD *a*-TiO_2 films were however not directly detectable by XPS.[4, 18] Hence, either the concentration of Ti^{3+} sites near the surface is below the detection limit of XPS, or such sites may not be present on the surface of air-exposed samples due to oxidation of Ti^{3+} in the presence of water and air.[4, 30, 53] The oxidation of surface Ti^{3+} sites would likely create a surface layer that is more resistive than the bulk of the film, consistent with the low conductance values measured when non-penetrative, soft contacts (e.g. Hg droplet or liquid electrolyte contacts) were made to the ALD-TiO_2 films. Deposition of metal contacts by electron-beam evaporation or sputtering would thus allow low-resistance contacts to be made to the ALD-

TiO_2,[4, 16] consistent with expectations for penetration of a native resistive surface layer on these *a*-TiO_2 films.

The *J-V* behavior for p^+-Si|TiO_2|Ni devices formed with TiO_2 from varied ALD processes shows that conduction through films of ALD *a*-TiO_2 is not limited to films produced from TDMAT, although the conductivity of *a*-TiO_2 formed using TDMAT is greater than for films formed using $TiCl_4$. Increases in the conductivities of the films correlated with increases in the strengths of the EPR signals for Ti^{3+} as well as with increases in the amplitude of the defect peak in the valence-band spectra. In combination, these data suggest that Ti^{3+} sites are important contributors to the conductivities of the films.

Previously, the high conductivities of TDMAT-TiO_2 films were hypothesized to directly arise from an increased density of C and N impurities.[4, 18] The C and N impurities were measured for all films (TDMAT, 150 ºC, 100 ºC and 50 ºC $TiCl_4$ films) via SIMS, which revealed very similar concentrations of C and N impurities in all of the samples despite the large range in observed film conductivity. The C and N impurities thus appear to be independent of the precursor and preparation of the *a*-TiO_2 film, unlike the concentration of Ti^{3+} sites. The normalized SIMS spectra for C and N are displayed in **Figure S9**.

B. Conduction through the *a*-TiO_2 Bulk

Temperature-Dependent Conductivity

The temperature-dependent conductivity for temperatures > 250 K of Ni|*a*-TiO_2|Ni layered stacks showed Arrhenius-type behavior, with an activation energy of 350 meV and a prefactor of ~ 0.4. The observed activation energy suggests a Marcus type of reorganization energy of 1.4 eV.[80] A transition was observed from Arrhenius-type behavior in the high-temperature limit (> 250 K) to temperature-independent tunneling type behavior at low

temperatures (< 50 K). Similar behavior has been observed with NiO.[81] In addition, analogous behavior has also been observed for sputtered TiO_2 films, even though the sputtered TiO_2 films had 3–4 orders of magnitude higher conductivities than the *a*-TiO_2 films produced herein.[82-83] For crystalline rutile and anatase TiO_2, small-polaron or variable-range hopping between Ti^{3+} sites and adjacent Ti^{4+} sites is most commonly thought to be the primary conduction mechanism, and theory has been used to model small-polaron hopping in both crystalline and amorphous TiO_2.[47, 57, 69, 84-86] Pham et al. have used DFT+U methods to calculate a reorganization energy for charge transfer between Ti^{3+} and Ti^{4+} sites in *a*-TiO_2 of 1.14 eV, while Deskins and Dupuis have used similar methods to estimate an activation energy for polaron hoping in both rutile and anatase TiO_2 of ~ 0.3 eV.[47, 72] Both estimates are consistent with the results reported herein.[47] Assuming that the density of Ti^{3+} sites is equal to the measured trap-site density (~10^{19} cm^{-3}) yields an average distance between Ti^{3+} sites of ~ 4 nm, whereas Ti–Ti distances in TiO_2 rutile or anatase crystals are 0.30 – 0.46 nm.[87-88]

Frequency-Dependent Conductivity

The AC conductivity of Ni|*a*-TiO_2|p^+-Si devices was constant (3.0×10^{-6} S cm^{-1}) for frequencies $\leqslant 10^5$ Hz, and increased rapidly for frequencies above 10^6 Hz. For charge transport within the conduction band or valence band of a semiconductor, the AC conductivity can be described by the Drude model,[44, 89-90]

$$\sigma(\omega) = \frac{\sigma_0}{1 + \omega^2\tau^2} \quad (7)$$

where σ_0 is the DC conductivity, ω is the AC radial frequency, and τ is the relaxation time. This model predicts a decrease in conductivity with increases in AC frequency, and hence is not consistent with the behavior reported herein.

For charge transport via hopping, isolated hopping sites do not contribute to the DC conductivity. However, as the frequency increases, these isolated hopping sites increasingly contribute to the AC conductivity. The frequency dependence of the conductivity in a wide variety of disordered materials obeys a power law,[91-94] and can be written as:

$$\sigma(\omega) = A\omega^s + \sigma_{DC} \quad (8)$$

where A is a constant, ω is the angular frequency, s is the exponent of the angular frequency, and σ_{DC} is the DC conductivity.[40] The data reported herein are consistent with this model, and a fit of the data to eq 8 yielded $A = 9.94 \times 10^{-17}$ S m^{-1} s$^{1.95}$, and $s = 1.95$ (**Figure 3**).

Potential-Dependent Conductivity

The potential-dependent conductivity measured by the EC-FET experiments showed only a 1% decrease in conductivity as the potential of the gate was moved positively toward the valence band of the TiO_2. If conduction across the *a*-TiO_2 relied upon electrons tunneling into the TiO_2 conduction band through a shallow space-charge region at the interface, then the EC-FET experiments would be expected to exhibit a strong dependence of the conductivity on the gate voltage. Specifically, a sharp decrease in conductivity would be observed at potentials positive of the conduction band of the *a*-TiO_2. The results are thus not consistent with conduction via tunneling of electrons into the conduction band of *a*-TiO_2.

The TiO_2 conductivity at positive potentials is sufficient to support faradaic current densities in the range of 10 mA cm^{-2} without substantially affecting the OER overpotential. As illustrated in **Figure S10**, for *a*-TiO_2 conductivities of ~ 10^{-5} S cm, the potential drop across the p^+-Si|*a*-TiO_2|Ni interface is smaller than the potential drop at the *a*-TiO_2|Ni|electrolyte interface. The simulation also shows that decreasing conductivity will affect the transport properties across the protecting layer, thus increasing the OER overpotential.

C. Conduction across *a*-TiO_2 Interfaces with Varied Metal Contacts

Contacts between *a*-TiO_2 and Ti ($\phi = 4.3 \pm 0.2$ eV) or Mg ($\phi = 3.7 \pm 0.2$ eV), which have smaller work functions than that of *a*-TiO_2 ($\phi = 4.7$ eV) and have mutually similar V_{FB} values, exhibited mutually similar *J-V* characteristics (**Figure 1**). Contacts between *a*-TiO_2 and Au ($\phi = 5.1 \pm 0.30$ eV), Pd ($\phi = 5.3 \pm 0.2$ eV), Ir ($\phi = 5.3 \pm 0.2$ eV), or Pt ($\phi = 5.6 \pm 0.07$ eV), which have work functions greater than that of the *a*-TiO_2, passed ≤ 10 % of the current densities of devices that have low-work-function top contacts. The contact between *a*-TiO_2 and Ni ($\phi = 5.1 \pm 0.4$ eV) was a notable exception, exhibiting *J-V* characteristics similar to those with low-work-function metals but with a work function similar to the aforementioned high-work-function contacts. Contacts to low-work-function metals moreover showed less resistance than contacts to high-work-function metals.

Some differences in the *J-V* behavior among the devices with high-work-function contacts were evident; specifically, at biases < 100 mV, devices with Pd contacts passed only ~ 10% of the current passed by devices with Au contacts. In decreasing order, devices with Au, Ir, Pt, Pd top contacts exhibited a reduction in current that matched (except for Pd) the order in which the work functions of the metal contacts increase (Au, Pd, Ir, Pt).

The work functions for the various clean metals were measured by UPS under high-vacuum conditions, whereas the conduction was measured for the e-beam deposited metal in contact with the TiO_2 substrate. Polycrystalline metals have multiple crystal faces exposed, so the measurements give an average over the various crystal faces. The averaging is expected to be different depending on the phenomena measured. Also, the fraction of each exposed face may not be the same for the clean metal compared to that of the metal sputtered onto a TiO_2

surface. Thus, only a rough correlation is expected between the work functions measured by UPS and the measured *J-V* behavior.

Space-charge limited current spectroscopy was used to determine the mobility and the trap density in the TDMAT *a*-TiO_2 films. The trap density and mobility were found for Au, Ir, Pt and Pd as well as Ir, Pt and Pd, respectively. As can be seen in **Figure 2b** and **Table S2**, the trap density and mobility were found to be 1×10^{19} cm^{-3} and $6.5 \pm 3 \times 10^{-4}$ cm^2 V^{-1} s^{-1}, respectively, and essentially independent of the top contact. The mobility value was used assumed to be independent of the top contact's work function and was thus used to determine the effective carrier concentration for all of the top contacts. The effective carrier concentration found using this mobility value is in agreement with the carrier concentration observed when measuring the carrier concentration by the Hall effect with In contacts (**Figure 2c)**. In addition, the mobility measured is in agreement with the predicted mobility found by DFT+U methods of 2×10^{-4} cm^2 V^{-1} s^{-1} by Pham et al.[47]

Devices with a top contact less than ~ 5.2 eV showed to have the (effective) free-carrier concentration of the device to be independent of the work function. Greater than the ~ 5.2 eV the devices' (effective) free-carrier concentration decreases by 10^1 - 10^2 cm^{-3} and is dependent on the work function. The former devices with contacts to metals that have work functions less than the work function of *a*-TiO_2 had the (effective) free-carrier concentrations on the order of 10^{16} cm^{-3}. Conversely, the effective free-carrier concentrations in the *a*-TiO_2 for devices with contacts greater than the work function of *a*-TiO_2 were ~ 10^{14} - 10^{15} cm^{-3}, again with the exception of Ni, which showed free-carrier concentrations similar to those measured for contacts with the low-work-function metals.

The dependence on the work function can consistently be ascribed to band-bending in the TiO_2 induced by the respective top contact. Metals with a work function greater than the Fermi-level of the *a*-TiO_2 bend the defect band away from the Fermi level, which will not change the occupancy of the defect band. Conversely, metals with a work function less than the Fermi-level of the *a*-TiO_2 will cause the defect band to bend towards, and even above the Fermi-level. With states above the Fermi-level, mobile charge-carriers (electrons) will empty these states, thus converting Ti^{3+} into Ti^{4+}.

These free-carrier concentrations are an effective average for the *a*-TiO_2, because the depletion width can extend through roughly half the thickness of the film. The conductivity of the *a*-TiO_2 correlates with the Ti^{3+} concentration in the *a*-TiO_2 films, so any local change to the Ti^{3+} concentration will affect the conductivity of the *a*-TiO_2

Conduction through the defect band can occur by hoping between sites (e.g. Ti^{4+}/Ti^{3+}). If defect sites exist above the Fermi level of the system, then those sites would have fewer free electrons that can hop between sites, and hence conduction is expected to be less favorable in that part of the band.

The *J-V* behavior of the films with different metal contacts is consistent with an equilibration process between the *a*-TiO_2 and the metal contact in conjunction with Fermi level pinning in the TiO_2. During equilibration, low-work-function metals (e.g. Mg, Ti) contacts inject electrons into the *a*-TiO_2, whereas high-work-function contacts extract electrons from the *a*-TiO_2. In this process, most of the electrons would be expected to come from, or enter, the near-surface states of the TiO_2 defect band that are responsible for the Fermi level pinning, thus the number of Ti^{3+} sites close to the surface remain the same or decrease.

The very low work functions of Mg and Ti suggest that the TiO_2 is forced into accumulation, primarily producing charge mostly on or near the surface, as opposed to substantial band bending. The Ti^{3+} defect sites would thus be available for conduction through the TiO_2. Alternatively, the noble metals, with high work functions, are expected to remove electrons from the near-surface states, and thus reduce the numbers of Ti^{3+} sites close to the surface.[16, 42] This process would produce bending of the defect band and Ti^{3+} sites at higher energy than the Fermi level would be lost, thus decreasing conduction through that part of the band. The near-surface states would be more affected, resulting in relatively few Ti^{3+} sites on the surface and thus forming a barrier to conduction between the TiO_2 and the metal.

Attempts have been made to observe the 'draining' of the defect band by both EPR and valence-band spectra. The density of states for any deposited metal would overlap and quickly overpower the Ti^{3+} signal for the valence band spectra, even for <1 nm of deposited metal. The analogous experiment for EPR was attempted using <10 nm of deposited metal. However, the small amount of metal was so strongly absorbing of the incoming microwaves that the instrument could not be tuned to collect the spectrum.

This simple band-bending picture does not fully explain the observations regarding changes in the measured *a*-TiO_2 film conductivity with different metal contacts. The work function of Ni (5.1 ± 0.4 eV) is greater than that of *a*-TiO_2 (4.7 eV) and closer to that of Au (5.1 ± 0.3 eV) than to Ti or Mg ($\leqslant$ 4.3 eV). Furthermore, the data support a wide dispersion in energy (~ 0.8 eV) for the defect band associated with Ti^{3+} states, which would allow a substantial density of defect states to remain below the *a*-TiO_2 Fermi level, for all high-work-function contacts examined herein. However, after subtraction of a Shirley-type background, the defect band peak was fitted with a Gauss-Lorentz peak profile with a 40% Gaussian contribution and

60% Lorentzian contribution. The obtained peak broadening of ~ 0.8 eV can thus be split into the 0.32 eV instrumental broadening (Gaussian) and 0.48 eV intrinsic lifetime broadening (Lorentzian).

Differences in chemical reactivity might also contribute to the observed differences in behavior of the metal contacts; specifically, noble metals (Au, Ir, Pt, and Pd) showed lower conduction across interfaces with *a*-TiO_2 than non-noble metals (Mg, In, Ti, Ni). Thus, the contact interface between the metal and the TiO_2 may also play a role in providing low resistance contacts. Ir, an active catalyst of the oxygen-evolution reaction in acidic electrolytes, does not form a highly conductive contact to *a*-TiO_2; however, deposition of an acid-stable metal (Ti) that does form a highly conductive contact to *a*-TiO_2 prior to deposition of the Ir catalyst allowed beneficial integration of the Ir catalyst with the *a*-TiO_2 coating, yielding photoanodes that exhibit high fill factors for water oxidation in 1.0 M H_2SO_4(aq).

In the expected behavior of Ni when comparing its work function to the work function of the *a*-TiO_2, it has been shown that the interface is not the source of the discrepancy. The Si|TiO_2|Ni|electrolyte interface has been probed via ambient pressure XPS.[17, 48] It has been shown that for ultra-thin layers of Ni (< 1 nm) no conduction was observed in $Fe(CN)_6^{3-/4-}$(aq) and 1.0 M KOH(aq). The conductivity and OER performance was observed and greatly increased for d_{Ni} > 1nm. For thin Ni layers under oxidative conditions, only oxidized Ni phases are expected (NiO_x, NiOOH is the catalyst phase, and under the OER conditions at pH 14 no metallic Ni can exist). However, small amounts of metallic Ni phases for d_{Ni} > 0.6 nm were observed (using AP-XPS under potential control in 1.0 M KOH(aq)) which increased in intensity for increased deposition of Ni. This behavior led to the proposed picture of a TiO_2|Ni|NiO_x structure under OER, analogous to the structure of a TiO_2|Ti interface.[48] Separate ex-situ UHV

measurements using different excitation energies and varying the electron emission angle confirmed the presence of a metallic Ni phase below the surface. In addition, cross-sectional TEM and SEM images of the TiO_2|Ni interface region further support the presence of metallic Ni at the interface of the TDMAT *a*-TiO_2.[4, 18]

The reason for Ni's divergence from the expected behavior is attributed to its work function. The work function of Ni although is more positive of the *a*-TiO_2, it is not sufficiently positive enough to cause a significant reduction of Ti^{3+} concentration at the interface but rather a slight reduction of the concentration at the interface due to the broad width of the Ti^{3+} defect band.

V. Conclusions

a-TiO_2 films deposited via ALD contained a broad (~ 0.8 eV) defect band between the TiO_2 Fermi level and TiO_2 valence band. For ALD TiO_2 films deposited under varied conditions and using varied precursors, the size of the defect band correlated with both the bulk conductivity of the *a*-TiO_2 films, and the Ti^{3+} concentration observed via EPR spectroscopy. In combination with a variety of solid-state measurements, including temperature-dependent conductivity, the data show that conduction through the bulk TiO_2 films is consistent with hopping mechanism between Ti^{3+} and adjacent Ti^{4+} sites as opposed to conduction via the conduction or valence bands. The wide defect band associated with Ti^{3+} sites spans an energy level comparable to the valence bands of light-absorbing semiconductors such as Si. Thus, allowing anodic conduction across that would otherwise present a ~ 2 eV barrier to anodic conduction.

The conduction across interfaces between metal contacts and *a*-TiO_2 films depended on the metal. For the metals examined, interfaces with metals having work functions less than *a*-TiO_2 generally provided higher conductivities than interfaces with metals having work functions greater than *a*-TiO_2. These observations are mostly consistent with a $Ti^{3+/4+}$ conduction that makes use of defect sites close to the surface both to reduce the band bending in the bulk of the TiO_2 and to provide either an insulating or conducting interface between the TiO_2 and the metal. Thus, for metals with low work function, a low resistance path is provided by Ti^{3+} sites, whereas for high work-function metals, the Ti^{3+} sites are depleted and the resistance consequently increases. Ni, while having a relatively high work function, acts like a low work function metal and thus constitutes a notable exception. Properties of the metal contact other than the work function may thus contribute to the different conductivities of interfaces with *a*-TiO_2. The observations provide guidance for a synergistic choice for contacts to *a*-TiO_2 films, showing that improved performance can be obtained for sunlight-driven water-oxidation using an n-Si|*a*-TiO_2 photoanode integrated with an Ir catalyst when a Ti interconnect is inserted between the *a*-TiO_2 and Ir catalyst relative to the situation in which the Ir catalyst is deposited directly onto the *a*-TiO_2.

Supporting Information

UPS measurements for various metals; normalized differential conductance from *J-V* data for p^+-Si|*a*-TiO_2|Ni device; measured contact resistances and respective compensating voltages; *J-V* data for SCLC measurement for p^+-Si|*a*-TiO_2 devices with Au, Ir and Pd top contacts; resulting parameters calculated from the SCLC measurement; absence of crystallinity in GIXRD and Raman measurements for all *a*-TiO_2 types; ATR-IR measurements for all *a*-TiO_2 types on different substrates; averaged Ti 2p XPS and valence band spectra for all types of *a*-TiO_2; EPR control experiments; resulting attenuation length for different take-off angles; Ti 2p XPS and valence band spectra at various take-off angles; normalized C and N SIMS spectra for all types of *a*-TiO_2; details on EC-FET measurement and results from samples measured

ACKNOWLEDGEMENTS

This work was supported through the Office of Science of the U.S. Department of Energy (DOE) under Award No. DE-SC0004993 to the Joint Center for Artificial Photosynthesis, a DOE Energy Innovation Hub. P.D.N. and C.W.R. thank support from the National Science Foundation for graduate research fellowships. C.W.R. also thanks the Link Energy Foundation for a graduate research fellowship. Research was in part carried out at the Molecular Materials Resource Center of the Beckman Institute and at the Microanalysis Center of the California Institute of Technology. D.J.F. acknowledges the financial support by the UK Engineering and Physical Sciences Research Council through the PVTEAM programme (EP/L017792/1). We thank Dr. Y. Guan for secondary-ion mass spectroscopy measurements; Dr. Angelo Di Bilio and Dr. Paul H. Oyala for EPR measurements; and K. Papadantonakis for assistance with editing this manuscript. S.H and S.J.K acknowledge start-up support from the Tomkat Foundation.

AUTHOR INFORMATION

Corresponding Authors

*E-mail: nslewis@caltech.edu (Nathan S. Lewis) shu.hu@yale.edu (Shu Hu)

steven.konezny@yale.edu (Steven J. Konezny)

Notes

The authors declare no competing financial interest.

VI. References

1. Pourbaix, M., *Atlas of Electrochemical Equilibria in Aqueous Solutions*, Second Edition ed.; National Association of Corrosion, 1974.

2. Lewis, N. S., Developing a Scalable Artificial Photosynthesis Technology Through Nanomaterials by Design. *Nat. Nanotechnol.* **2016**, *11*, 1010-1019.

3. Haussener, S.; Hu, S.; Xiang, C.; Weber, A. Z.; Lewis, N. S., Simulations of the Irradiation and Temperature Dependence of the Efficiency of Tandem Photoelectrochemical Water-Splitting Systems. *Energy Environ. Sci.* **2013**, *6*, 3605.

4. Hu, S.; Shaner, M. R.; Beardslee, J. A.; Lichterman, M.; Brunschwig, B. S.; Lewis, N. S., Amorphous TiO_2 Coatings Stabilize Si, GaAs, and GaP Photoanodes for Efficient Water Oxidation. *Science* **2014**, *344*, 1005-1009.

5. Shaner, M. R.; Hu, S.; Sun, K.; Lewis, N. S., Stabilization of Si Microwire Arrays for Solar-Driven H_2O Oxidation to O_2(g) in 1.0 M KOH(aq) Using Conformal Coatings of Amorphous TiO_2. *Energy Environ. Sci.* **2015**, *8*, 203-207.

6. Sun, K.; McDowell, M. T.; Nielander, A. C.; Hu, S.; Shaner, M. R.; Yang, F.; Brunschwig, B. S.; Lewis, N. S., Stable Solar-Driven Water Oxidation to O_2(g) by Ni-Oxide Coated Silicon Photoanodes. *J. Phys. Chem. Lett.* **2015**, *6*, 592-598.

7. Chen, Y. W.; Prange, J. D.; Dühnen, S.; Park, Y.; Gunji, M.; Chidsey, C. E. D.; McIntyre, P. C., Atomic Layer-Deposited Tunnel Oxide Stabilizes Silicon Photoanodes for Water Oxidation. *Nat. Mater.* **2011**, *10*, 539-544.

8. Kainthla, R. C.; Zelenay, B.; Bockris, J. O. M., Protection of n-Si Photoanode Against Photocorrosion in Photoelectrochemical Cell for Water Electrolysis. *J. Electrochem. Soc.* **1986**, *133*, 248-253.

9. Kenney, M. J.; Gong, M.; Li, Y.; Wu, J. Z.; Feng, J.; Lanza, M.; Dai, H., High-Performance Silicon Photoanodes Passivated with Ultrathin Nickel Films for Water Oxidation. *Science* **2013**, *342*, 836-840.

10. Mei, B.; Seger, B.; Pedersen, T.; Malizia, M.; Hansen, O.; Chorkendorff, I.; Vesborg, P. C. K., Protection of p^+-n-Si Photoanodes by Sputter-Deposited Ir/IrO_x Thin Films. *J. Phys. Chem. Lett.* **2014**, *5*, 1948-1952.

11. Yang, J., et al., Efficient and Sustained Photoelectrochemical Water Oxidation by Cobalt Oxide/Silicon Photoanodes with Nanotextured Interfaces. *J. Am. Chem. Soc.* **2014**, *136*, 6191-4.

12. Zhou, X.; Liu, R.; Sun, K.; Papadantonakis, K. M.; Brunschwig, B. S.; Lewis, N. S., 570 mV Photovoltage, Stabilized n-Si/CoO_x Heterojunction Photoanodes Fabricated Using Atomic Layer Deposition. *Energy Environ. Sci.* **2016**, *9*, 892-897.

13. McDowell, M. T.; Lichterman, M. F.; Spurgeon, J. M.; Hu, S.; Sharp, I. D.; Lewis, N. S., Improved Stability of Polycrystalline Bismuth Vanadate Photoanodes by Use of Dual-Layer Thin TiO_2/Ni Coatings. *J. Phys. Chem. C* **2014**, *118*, 19618-19624.

14. Lichterman, M. F.; Carim, A. I.; McDowell, M. T.; Hu, S.; Gray, H. B.; Brunschwig, B. S.; Lewis, N. S., Stabilization of n-Cadmium Telluride Photoanodes for Water Oxidation to O_2(g) in Aqueous Alkaline Electrolytes Using Amorphous TiO_2 Films Formed by Atomic-Layer Deposition. *Energy Environ. Sci.* **2014**, *7*, 3334-3337.

15. Kohl, P. A.; Frank, S. N.; Bard, A. J., Semiconductor Electrodes XI. Behavior of n- and p-Type Single-Crystal Semiconductors Covered with Thin Normal-TiO_2 Films. *J. Electrochem. Soc.* **1977**, *124*, 225-229.

16. Hu, S.; Richter, M. H.; Lichterman, M. F.; Beardslee, J.; Mayer, T.; Brunschwig, B. S.; Lewis, N. S., Electrical, Photoelectrochemical, and Photoelectron Spectroscopic Investigation of the Interfacial Transport and Energetics of Amorphous TiO_2/Si Heterojunctions. *J. Phys. Chem. C* **2016**, *120*, 3117-3129.

17. Lichterman, M. F., et al., Direct Observation of the Energetics at a Semiconductor/Liquid Junction by Operando X-Ray Photoelectron Spectroscopy. *Energy Environ. Sci.* **2015**, *8*, 2409-2416.

18. McDowell, M. T.; Lichterman, M. F.; Carim, A. I.; Liu, R.; Hu, S.; Brunschwig, B. S.; Lewis, N. S., The Influence of Structure and Processing on the Behavior of TiO_2 Protective

Layers for Stabilization of n-Si/TiO_2/Ni Photoanodes for Water Oxidation. *ACS Appl. Mater. Interfaces* **2015**, *7*, 15189-15199.

19. Bae, D.; Shayestehaminzadeh, S.; Thorsteinsson, E. B.; Pedersen, T.; Hansen, O.; Seger, B.; Vesborg, P. C. K.; Ólafsson, S.; Chorkendorff, I., Protection of Si Photocathode Using TiO_2 Deposited by High Power Impulse Magnetron Sputtering for H_2 Evolution in Alkaline Media. *Sol. Energy Mater. Sol. Cells* **2016**, *144*, 758- 765.

20. Seger, B.; Pedersen, T.; Laursen, A. B.; Vesborg, P. C.; Hansen, O.; Chorkendorff, I., Using TiO_2 as a Conductive Protective Layer for Photocathodic H_2 Evolution. *J. Am. Chem. Soc.* **2013**, *135*, 1057-1064.

21. Seger, B.; Tilley, D. S.; Pedersen, T.; Vesborg, P. C. K.; Hansen, O.; Grätzel, M.; Chorkendorff, I., Silicon Protected with Atomic Layer Deposited TiO_2: Durability Studies of Photocathodic H_2 Evolution. *RSC Adv.* **2013**, *3*, 25902.

22. Mei, B.; Pedersen, T.; Malacrida, P.; Bae, D.; Frydendal, R.; Hansen, O.; Vesborg, P. C.; Seger, B.; Chorkendorff, I., Crystalline TiO_2: A Generic and Effective Electron-Conducting Protection Layer for Photoanodes and Cathodes. *J. Phys. Chem. C* **2015**, *119*, 15019-15027.

23. Li, M.; Hebenstreit, W.; Diebold, U.; Tyryshkin, A. M.; Bowman, M. K.; Dunham, G. G.; Henderson, M. A., The Influence of the Bulk Reduction State on the Surface Structure and Morphology of Rutile TiO_2(110) Single Crystals. *The Journal of Physical Chemistry B* **2000**, *104*, 4944-4950.

24. Su, J.; Zou, X.-X.; Zou, Y.-C.; Li, G.-D.; Wang, P.-P.; Chen, J.-S., Porous Titania with Heavily Self-Doped Ti^{3+} for Specific Sensing of CO at Room Temperature. *Inorg Chem* **2013**, *52*, 5924-5930.

25. Khomenko, V.; Langer, K.; Rager, H.; Fett, A., Electronic Absorption by Ti^{3+} Ions and Electron Delocalization in Synthetic Blue Rutile. *Phys Chem Miner* **1998**, *25*, 338-346.

26. Amano, F.; Nakata, M.; Yamamoto, A.; Tanaka, T., Effect of Ti^{3+} Ions and Conduction Band Electrons on Photocatalytic and Photoelectrochemical Activity of Rutile Titania for Water Oxidation. *J. Phys. Chem. C* **2016**, *120*, 6467-6474.

27. Chen, X.; Liu, L.; Peter, Y. Y.; Mao, S. S., Increasing Solar Absorption for Photocatalysis with Black Hydrogenated Titanium Dioxide Nanocrystals. *Science* **2011**, *331*, 746-750.

28. Zuo, F.; Wang, L.; Wu, T.; Zhang, Z.; Borchardt, D.; Feng, P., Self-Doped Ti^{3+} Enhanced Photocatalyst for Hydrogen Production Under Visible Light. *J. Am. Chem. Soc.* **2010**, *132*, 11856-11857.

29. Xing, M.; Fang, W.; Nasir, M.; Ma, Y.; Zhang, J.; Anpo, M., Self-Doped Ti^{3+}-Enhanced TiO_2 Nanoparticles with a High-Performance Photocatalysis. *J. Catal.* **2013**, *297*, 236-243.

30. Hoang, S.; Berglund, S. P.; Hahn, N. T.; Bard, A. J.; Mullins, C. B., Enhancing Visible Light Photo-oxidation of Water with TiO_2 Nanowire Arrays via Cotreatment with H_2 and NH_3: Synergistic Effects Between Ti^{3+} and N. *J. Am. Chem. Soc.* **2012**, *134*, 3659-3662.

31. Verlage, E.; Hu, S.; Liu, R.; Jones, R. J. R.; Sun, K.; Xiang, C.; Lewis, N. S.; Atwater, H. A., A Monolithically Integrated, Intrinsically Safe, 10% Efficient, Solar-Driven Water-Splitting System Based on Active, Stable Earth-Abundant Electrocatalysts in Conjunction with Tandem III–V Light Absorbers Protected by Amorphous TiO_2 Films. *Energy Environ. Sci.* **2015**, *8*, 3166-3172.

32. Piercy, B. D.; Losego, M. D., Tree-Based Control Software for Multilevel Sequencing in Thin Film Deposition Applications. *J. Vac. Sci. Technol. B.* **2015**, *33*, 043201.

33. Plana, D.; Humphrey, J.; Bradley, K.; Celorrio, V.; Fermín, D., Charge Transport Across High Surface Area Metal/Diamond Nanostructured Composites. *ACS Appl. Mater. Interfaces* **2013**, *5*, 2985-2990.

34. Roest, A.; Kelly, J.; Vanmaekelbergh, D.; Meulenkamp, E., Staircase in the Electron Mobility of a ZnO Quantum Dot Assembly Due to Shell Filling. *Phys. Rev. Lett.* **2002**, *89*, 036801.

35. Olthuis, W.; Streekstra, W.; Bergveld, P., Theoretical and Experimental-Determination of Cell Constants of Planar-Interdigitated Electrolyte Conductivity Sensors. *Sens. Actuators, B* **1995**, *24*, 252-256.

36. Michaelson, H. B., The Work Function of the Elements and Its Periodicity. *J. Appl. Phys.* **1977**, *48*, 4729-4733.

37. Hofmann, T.; Yu, T. H.; Folse, M.; Weinhardt, L.; Bar, M.; Zhang, Y. F.; Merinov, B. V.; Myers, D. J.; Goddard, W. A.; Heske, C., Reply to "Comment on 'Using Photoelectron Spectroscopy and Quantum Mechanics to Determine d-Band Energies of Metals for Catalytic Applications'". *Journal of Physical Chemistry C* **2013**, *117*, 6916-6917.

38. Hofmann, T.; Yu, T. H.; Folse, M.; Weinhardt, L.; Bar, M.; Zhang, Y. F.; Merinov, B. V.; Myers, D. J.; Goddard, W. A.; Heske, C., Using Photoelectron Spectroscopy and Quantum Mechanics to Determine d-Band Energies of Metals for Catalytic Applications. *Journal of Physical Chemistry C* **2012**, *116*, 24016-24026.

39. Chiu, F. C., A Review on Conduction Mechanisms in Dielectric Films. *Adv. Mater. Sci. Eng.* **2014**.

40. Bottger, H.; Bryksin, V. V., *Hopping Conduction in Solids*; Akademie-Verlag Berlin, 1985.

41. Rose, A., Space-Charge-Limited Currents in Solids. *Phys. Rev.* **1955**, *97*, 1538.

42. Tredgold, R. H., *Space Charge Conduction in Solids*; Elsevier Pub. Co., 1966.

43. Kim, S.; Jeong, H. Y.; Choi, S. Y.; Choi, Y. K., Comprehensive Modeling of Resistive Switching in the Al/TiO_x/TiO_2/Al Heterostructure Based on Space-Charge-Limited Conduction. *Appl. Phys. Lett.* **2010**, *97*.

44. Kao, K.-C.; Hwang, W., *Electrical Transport in Solids: with Particular Reference to Organic Semiconductors*
, 1st ed.; Pergamon Press: Oxford ; New York, 1981.

45. Riviere, J., Work Function: Measurements and Results. In *Solid State Surface Science*, Green, M., Ed. Decker: New York, 1969; Vol. 1, pp 179–289.

46. Hölzl, J.; Schulte, F. K., Work Function of Metals. In *Solid Surface Physics*, Höhler, G., Ed. Springer-Verlag: Berlin, 1979; pp 1-150.

47. Pham, H. H.; Wang, L. W., Oxygen Vacancy and Hole Conduction in Amorphous TiO_2. *Phys. Chem. Chem. Phys.* **2015**, *17*, 541-550.

48. Lichterman, M. F., et al., An Electrochemical, Microtopographical and Ambient Pressure X-Ray Photoelectron Spectroscopic Investigation of Si/TiO_2/Ni/Electrolyte Interfaces. *J. Electrochem. Soc.* **2016**, *163*, H139 - H146.

49. Niilisk, A.; Moppel, M.; Pärs, M.; Sildos, I.; Jantson, T.; Avarmaa, T.; Jaaniso, R.; Aarik, J., Structural Study of TiO_2 Thin Films by Micro-Raman Spectroscopy. *Open Physics* **2006**, *4*, 105-116.

50. Piercy, B. D.; Leng, C. Z.; Losego, M. D., Variation in the Density, Optical Polarizabilities, and Crystallinity of TiO_2 Thin Films Deposited Via Atomic Layer Deposition

From 38 to 150° C Using the Titanium Tetrachloride-Water Reaction. *J. Vac. Sci. Technol., A* **2017**, *35*, 03E107.

51. Suriye, K.; Jongsomjit, B.; Satayaprasert, C.; Praserthdam, P., Surface Defect (Ti^{3+}) Controlling in the First Step on the Anatase TiO_2 Nanocrystal by Using Sol-Gel Technique. *Appl. Surf. Sci.* **2008**, *255*, 2759-2766.

52. Suriye, K.; Praserthdam, P.; Jongsomjit, B., Impact of Ti^{3+} Present in Titania on Characteristics and Catalytic Properties of the Co/TiO_2 Catalyst. *Ind. Eng. Chem. Res.* **2005**, *44*, 6599-6604.

53. Howe, R. F.; Gratzel, M., EPR Observation of Trapped Electrons in Colloidal Titanium Dioxide. *J. Phys. Chem.* **1985**, *89*, 4495-4499.

54. Reddy, S. L.; Reddy, G. S.; Endo, T., *Electronic (Absorption) Spectra of 3d Transition Metal Complexes*; INTECH, 2012.

55. Fu, G.; Zhou, P.; Zhao, M. M.; Zhu, W. D.; Yan, S. C.; Yu, T.; Zou, Z. G., Carbon Coating Stabilized Ti^{3+}-Doped TiO_2 for Photocatalytic Hydrogen Generation Under Visible Light Irradiation. *Dalton Trans.* **2015**, *44*, 12812-12817.

56. Liu, H.; Ma, H.; Li, X.; Li, W.; Wu, M.; Bao, X., The Enhancement of TiO_2 Photocatalytic Activity by Hydrogen Thermal Treatment. *Chemosphere* **2003**, *50*, 39-46.

57. Yildiz, A.; Iacomi, F.; Mardare, D., Polaron Transport in TiO_2 Thin Films. *J. Appl. Phys.* **2010**, *108*, 083701.

58. Wendt, S.; Sprunger, P. T.; Lira, E.; Madsen, G. K.; Li, Z.; Hansen, J. Ø.; Matthiesen, J.; Blekinge-Rasmussen, A.; Lægsgaard, E.; Hammer, B., The Role of Interstitial Sites in the Ti3d Defect State in the Band Gap of Titania. *Science* **2008**, *320*, 1755-1759.

59. Schierbaum, K.-D.; Fischer, S.; Wincott, P.; Hardman, P.; Dhanak, V.; Jones, G.; Thornton, G., Electronic Structure of Pt Overlayers on (1×3) Reconstructed TiO_2 (100) Surfaces. *Surf. Sci.* **1997**, *391*, 196-203.

60. Linderälv, C.; Lindman, A.; Erhart, P., A Unifying Perspective on Oxygen Vacancies in Wide Band Gap Oxides. *J. Phys. Chem. Lett.* **2018**, *9*, 222-228.

61. Henkel, K.; Das, C.; Kot, M.; Schmeißer, D.; Naumann, F.; Kärkkänen, I.; Gargouri, H., In-Gap States in Titanium Dioxide and Oxynitride Atomic Layer Deposited Films. *J. Vac. Sci. Technol., A* **2017**, *35*, 01B135.

62. Das, C.; Richter, M.; Tallarida, M.; Schmeißer, D., Electronic Properties of Atomic Layer Deposition Films, Anatase and Rutile TiO_2 Studied by Resonant Photoemission Spectroscopy. *J. Phys. D: Appl. Phys.* **2016**, *49*, 275304.

63. Park, S.-J.; Lee, J.-P.; Jang, J. S.; Rhu, H.; Yu, H.; You, B. Y.; Kim, C. S.; Kim, K. J.; Cho, Y. J.; Baik, S., In Situ Control of Oxygen Vacancies in TiO_2 by Atomic Layer Deposition for Resistive Switching Devices. *Nanotechnology* **2013**, *24*, 295202.

64. Zhang, Y.; Ding, Z.; Foster, C. W.; Banks, C. E.; Qiu, X.; Ji, X., Oxygen Vacancies Evoked Blue TiO_2 (B) Nanobelts with Efficiency Enhancement in Sodium Storage Behaviors. *Adv. Funct. Mater.* **2017**, *27*, 1700856.

65. Di Valentin, C.; Pacchioni, G.; Selloni, A., Reduced and n-Type Doped TiO_2: Nature of Ti^{3+} Species. *J. Phys. Chem. C* **2009**, *113*, 20543-20552.

66. Deskins, N. A.; Dupuis, M., Intrinsic Hole Migration Rates in TiO_2 from Density Functional Theory. *J. Phys. Chem. C* **2009**, *113*, 346 - 358.

67. Deskins, N. A.; Rousseau, R.; Dupuis, M., Localized Electronic States from Surface Hydroxyls and Polarons in TiO_2 (110). *J. Phys. Chem. C* **2009**, *113*, 14583-14586.

68. Deskins, N. A.; Rousseau, R.; Dupuis, M., Distribution of Ti^{3+} Surface Sites in Reduced TiO_2. *J. Phys. Chem. C* **2011**, *115*, 7562-7572.

69. Deskins, N. A.; Rousseau, R.; Dupuis, M., Defining the Role of Excess Electrons in the Surface Chemistry of TiO_2. *J. Phys. Chem. C* **2010**, *114*, 5891 - 5897.

70. Xia, T.; Zhang, Y.; Murowchick, J.; Chen, X., Vacuum-Treated Titanium Dioxide Nanocrystals: Optical Properties, Surface Disorder, Oxygen Vacancy, and Photocatalytic Activities. *Catal Today* **2014**, *225*, 2-9.

71. Morgan, B. J.; Watson, G. W., Intrinsic n-Type Defect Formation in TiO_2: A Comparison of Rutile and Anatase from GGA+ U Calculations. *J. Phys. Chem. C* **2010**, *114*, 2321-2328.

72. Deskins, N. A.; Dupuis, M., Electron Transport via Polaron Hopping in Bulk TiO_2: A Density Functional Theory Characterization. *Phys Rev B* **2007**, *75*.

73. Nakamura, I.; Negishi, N.; Kutsuna, S.; Ihara, T.; Sugihara, S.; Takeuchi, K., Role of Oxygen Vacancy in the Plasma-Treated TiO_2 Photocatalyst with Visible Light Activity for NO Removal. *J. Mol. Catal. A: Chem.* **2000**, *161*, 205-212.

74. Diebold, U., The Surface Science of Titanium Dioxide. *Surf. Sci. Rep.* **2003**, *48*, 53-229.

75. Fukui, K.-i.; Onishi, H.; Iwasawa, Y., Atom-Resolved Image of the TiO_2 (110) Surface by Noncontact Atomic Force Microscopy. *Phys. Rev. Lett.* **1997**, *79*, 4202.

76. Jin, C.; Liu, B.; Lei, Z.; Sun, J., Structure and Photoluminescence of the TiO_2 Films Grown by Atomic Layer Deposition Using Tetrakis-Dimethylamino Titanium and Ozone. *Nanoscale research letters* **2015**, *10*, 95.

77. Saha, D.; Ajimsha, R.; Rajiv, K.; Mukherjee, C.; Gupta, M.; Misra, P.; Kukreja, L., Spectroscopic Ellipsometry Characterization of Amorphous and Crystalline TiO_2 Thin Films Grown by Atomic Layer Deposition at Different Temperatures. *Appl. Surf. Sci.* **2014**, *315*, 116-123.

78. Hashimoto, S.; Tanaka, A., Alteration of Ti 2p XPS Spectrum for Titanium Oxide by Low-Energy Ar Ion Bombardment. *Surf. Interface Anal.* **2002**, *34*, 262-265.

79. Mott, N., Electrons in Non-Crystalline Materials: The Last Twenty Five Years. *Contemp. Phys.* **1985**, *26*, 203.

80. Brunschwig, B. S.; Sutin, N., Energy Surfaces, Reorganization Energies, and Coupling Elements in Electron Transfer. *Coordin Chem Rev* **1999**, *187*, 233-254.

81. Austin, I. G.; Mott, N. F., Polarons in Crystalline and Non-Crystalline Materials. *Adv. Phys.* **2001**, *50*, 757-812.

82. Yildiz, A.; Lisesivdin, S.; Kasap, M.; Mardare, D., Electrical Properties of TiO_2 Thin Films. *J. Non-Cryst. Solids* **2008**, *354*, 4944-4947.

83. Austin, I. G.; Mott, N. F., Polarons in Crystalline and Non-Crystalline Materials. *Adv. Phys.* **1969**, *18*.

84. Liu, T.; Dupuis, M.; Li, C., Band Structure Engineering: Insights from Defects, Band Gap, and Electron Mobility, from Study of Magnesium Tantalate. *J. Phys. Chem. C* **2016**, *120*, 6930 - 6937.

85. Ju, Y.; Wang, M.; Wang, Y.; Wang, S.; Fu, C., Electrical Properties of Amorphous Titanium Oxide Thin Films for Bolometric Application. *Adv. Condens. Matter Phys.* **2013**, *2013*, 1 - 5.

86. Rao, M. V. R.; Gandhi, Y.; Rao, L. S.; Sahayabaskaran, G.; Veeraiah, N., Electrical and Spectroscopic Properties of $LiF–Bi_2O_3–P_2O_5$:TiO_2 Glass System. *Mater. Chem. Phys.* **2011**, *126*, 58 - 68.

87. Sugiyama, K.; Takeuchi, Y., The Crystal Structure of Rutile as a Function of Temperature up to 1600º C. *Z. Kristallogr. Cryst. Mater.* **1991**, *194*, 305-313.

88. Howard, C. J.; Sabine, T. M.; Dickson, F., Structural and Thermal Parameters for Rutile and Anatase. *Acta Crystallogr. Sec. B* **1991**, *47*, 462-468.

89. Ihle, D.; Lorenz, B., Small-Polaron Conduction and Short-Range Order in Fe_3O_4. *J. Phys. C: Solid State Phys.* **1986**, *19*, 5239-5251.

90. Mott, N. F.; Davis, E. A., *Electronic Processes in Non-Crystalline Materials*, 2nd ed.; Clarendon Press: Oxford,, 1979.

91. Jonscher, A. K., Universal Dielectric Response. *Nature* **1977**, *267*, 673-679.

92. Long, A. R., Frequency-Dependent Loss in Amorphous-Semiconductors. *Adv. Phys.* **1982**, *31*, 553-637.

93. Konezny, S. J.; Richter, C.; Snoeberger, R. C.; Parent, A. R.; Brudvig, G. W.; Schmuttenmaer, C. A.; Batista, V. S., Fluctuation-Induced Tunneling Conductivity in Nanoporous TiO_2 Thin Films. *J. Phys. Chem. Lett.* **2011**, *2*, 1931-1936.

94. Elliott, S. R., AC Conduction in Amorphous-Chalcogenide and Pnictide Semiconductors. *Adv. Phys.* **1987**, *36*, 135-218.

TOC Graphic: